

**MODELING OF NEEDLE INSERTION FORCES  
FOR PERCUTANEOUS THERAPIES**

by  
Christina Simone

A thesis submitted to The Johns Hopkins University in conformity with  
the requirements for the degree of Master of Science in Engineering

Baltimore, Maryland  
May, 2002

© Christina Simone 2002  
All rights reserved

## **Abstract**

This thesis reports on a method for modeling data from needle insertions into soft tissue. Force information from needle insertions was measured and modeled for use in robot-assisted percutaneous therapies. The goal of the work reported here was to develop a new methodology for reality-based data modeling that results in more accurate representation of a needle insertion scenario that could be used as a holistic relative position guide during percutaneous procedures. Insertion force data was collected on bovine livers using the Johns Hopkins University Steady-Hand Robot, and modeled in three parts: force due to capsule stiffness, friction, and cutting. Capsule stiffness is modeled by a nonlinear spring model, friction by a modified Karnopp model, and cutting by the remaining forces, which appear to be constant for a given tissue sample. During robot-assisted procedures, real-time force data can be compared to these models to control puncture of interior structures. Clinical applications of this work include liver ablation, biopsies, and prostate brachytherapy.

### **Advisor:**

Allison M. Okamura, Ph.D.

Professor, Department of Mechanical Engineering, Secondary Appt. in Computer Science

Johns Hopkins University

## Acknowledgements

This project provided an excellent opportunity for me to gain experience in several exciting new areas in my field. It was an extraordinary learning experience to encounter and overcome the numerous difficulties that arise in research. I wish to extend great thanks and appreciation to my advisor, Dr. Allison Okamura for the guidance and assistance she has provided to me. Friction modeling software was provided by Dr. Christopher Richard of Stanford University. Thanks to Dr. Gabor Fichtinger for advice in the area of percutaneous therapy. I would also like to thank Dr. Rajesh Kumar and Dr. Andy Bzostek for sharing their knowledge of the Steady-Hand Robot. For assistance with technical difficulties, I appreciate the aid of Dr. Darius Burschka and Anton Deguet. I also thank John Woomer for assistance in machining parts and offering suggestions on my designs. I am grateful to CT technicians Philip Keller and Robert M. Kain III for being kind enough to stay late, enabling me to gather data with the CT Fluoro machine. I appreciate the kindness of Panadda (Nim) Marayong and Arne Backes to take the time to make drives to obtain livers, assist me in a few experiments and brainstorm with me in stressful moments. Lastly, I thank my parents, Maria and Franco Simone, my brother Alessandro, and the rest of my friends not mentioned above for their encouragement and support.

My advisor and I also wish to acknowledge the support of the National Science Foundation under the Engineering Research Center grant #EEC9731478 and supplementary grant #EEC0121940.

# Table of Contents

Abstract .....	ii
Acknowledgements .....	iii
Table of Contents .....	iv
List of Tables.....	vi
List of Figures .....	vii
1    Introduction .....	1
1.1    Motivation.....	1
1.2    General Background.....	4
1.3    Thesis Contributions .....	5
1.4    Organization.....	6
2    Experimental Equipment.....	7
2.1    Steady-Hand Robot .....	7
2.2    Needle Fixture.....	8
2.3    Force Sensor Mounting Flange .....	10
2.4    Force Sensor.....	10
2.5    Friction Experiment Platform.....	13
2.6    Control Software .....	14
3    Liver Experiments .....	17
3.1    Overall Stiffness.....	17
3.2    Internal Stiffness / Cutting .....	18
3.3    Friction and Damping.....	20

3.4	Stiffness Under CT Fluoro Imaging.....	22
3.5	Friction and Damping Under CT Fluoro Imaging .....	24
4	Data Analysis for Liver.....	27
4.1	Property Estimation.....	27
4.1.1	<i>Stiffness / Puncture</i> .....	29
4.1.2	<i>Friction / Damping</i> .....	36
4.1.3	<i>Cutting</i> .....	48
4.2	Model Validation.....	50
5	Prostate Experiment .....	52
5.1	Data Discussion.....	53
6	Conclusion.....	55
6.1	Contributions.....	56
6.2	Future Work .....	56
	Appendix A: Mechanical Drawings.....	59
	A.1 Needle Holder.....	59
	A.2 Top Plate.....	59
	A.2 Top Plate.....	60
	A.3 Force Sensor Mounting Flange .....	61
	Appendix B: Data Sheets .....	62
	B.1 INA103 Instrumentation Amplifier .....	62
	Appendix C: CT Fluoro Images.....	75
	Bibliography .....	76
	Curriculum Vita.....	80

## List of Tables

Table 1.	PID gains for each of the robot controllers.....	8
Table 2.	Values of the estimated pre-puncture nonlinear stiffness parameters ( $a_1, a_2$ ) for each liver.....	33
Table 3.	Values of the nonlinear stiffness parameters ( $a_1, a_2$ ) for internal stiffness measurements.....	35
Table 4.	Estimated friction parameters for liver 3. The experiment was performed without the use of imaging.....	46
Table 5.	Estimated friction parameters for liver 7. The experiment was performed under CT Fluoro imaging.....	4

## List of Figures

Figure 1. Data is acquired with a robotic system and used to create reality-based models for later use in haptic simulation, robotic assistance, or autonomous procedures.....	3
Figure 2. The Johns Hopkins University Steady-Hand Robot.....	7
Figure 3. The delrin needle fixture with needle and force sensor.....	9
Figure 4. Delrin halves of the needle fixture.....	9
Figure 5. (a) Top plate for Bokam sensor. (b) Top plate for Entran sensor with HeliCoil insert.....	9
Figure 6. The force sensor mounting flange.....	10
Figure 7. Two BOKAM™ force sensors.....	10
Figure 8. The EntranTM force sensor.....	11
Figure 9. Circuit diagram for connections from the load cell output to the amplifier circuit and power supply.....	12
Figure 10. (a) Original friction experiment platform. (b) Friction experiment platform after modifications for the CT Fluoro experiment.....	14
Figure 11. The graphical user interface developed for the experiments.....	16
Figure 12. The data acquisition system was comprised of the JHU Steady-Hand Robot, a needle holder with load cell, and a control computer.....	19
Figure 13. The capsule of the liver being removed from the surface.....	20
Figure 14. Friction experiment setup with the Steady-Hand Robot.....	21

Figure 15. Graphical representation of the sinusoidal motion of the needle during friction experiments.....	22
Figure 16. An image of the CT Fluoro console during a typical needle insertion (taken from digital video recordings).....	23
Figure 17. Stiffness experiments under CT Fluoro imaging.....	24
Figure 18. The setup for friction experiments under CT Fluoro imaging.....	26
Figure 19. Friction setup in the CT Fluoro machine.....	27
Figure 20. A typical force vs. position plot showing insertion and removal forces, and events such as puncture.....	28
Figure 21. Three-dimensional representation of one liver lobule, which includes many interior structures, (left, adapted from [13]), and a cutaway of one of the livers used in the experiments, revealing large interior vessels (right).....	29
Figure 22. Locations of the tissue surface at different stages of needle insertion. (a) pre-puncture (b) puncture (c) post-puncture.....	31
Figure 23. Typical stiffness data for a bovine liver before membrane puncture within a $10 \text{ cm}^2$ area.....	32
Figure 24. The two types of needle tips used in experiments. (a) A beveled Quincke point spinal needle. (b) A diamond point needle.....	33
Figure 25. Typical force data for an insertion into liver with a diamond tip needle. A pre-puncture event is evident.....	34
Figure 26. Maxwell body [Fung, 6].....	35
Figure 27. Voigt body. [Fung, 6].....	35
Figure 28. Kelvin body. [Fung, 6].....	36

Figure 29. Indentation of a semi-infinite elastic body with a rigid, right circular punch, [Ottensmeyer, 13].....	36
Figure 30. (a) The Karnopp friction model (adapted from [18]). (b) The modified Karnopp friction model (adapted from [18]).....	38
Figure 31. One period of force versus time data with segments highlighted.....	40
Figure 32. Images of the CT Fluoro console during a periodic needle insertion into liver. An enlarged version can be found in Appendix C.....	41
Figure 33. Free-body diagram of the system.....	43
Figure 34. Friction data for sinusoidal motion of the needle through a 1.95 cm thick liver sample at 0.2 Hz. (a) Velocity and force versus time. (b) Force versus velocity for the orginal data and the modified Karnopp friction model.....	45
Figure 35. Force model with actual data. Phases are highlighted.....	45
Figure 36. Forces on the needle tip during insertion. The point at which the entire liver lobe is punctured is denoted. Note the gradual upward slope in forces after this point.....	49
Figure 37. Forces on the needle during insertion with the average cutting force value marked.....	50
Figure 38. The needle insertion model is compared to two insertions on real livers. Although the general shape is similar, the model cannot exactly match the data because of the wide variation in insertion forces and collisions with unmodeled internal strctures.....	52
Figure 39. Data acquisition on a canine cadaver prostate.....	54

Figure 40. A complete plot of needle insertion forces on a canine prostate. There are  
several internal punctures..... 55

# 1 Introduction

## 1.1 Motivation

Percutaneous therapies are diagnostic or therapy delivery procedures that involve the insertion of tubular delivery devices into targeted locations in the body with the aid of intra-operative imaging devices (e.g., CT, MRI, ultrasound, and fluoroscopy). These delivery apparatuses include instruments such as needles, trocars, bone drills, screws, laser devices, etc. While minimally invasive surgery reduces patient discomfort and decreases recovery time, a major shortcoming is reduced visual and tactile information transmitted to the physician via the instruments. Current clinical methods involve an iterative manual technique of imaging and positioning, which lacks real-time presentation of information to the operator. In these procedures, it is often the case that sharp surgical instruments, such as needles, come into close proximity to delicate structures that are easily damaged. For example, the prostate lies next to the bladder, and the urethra runs through it. In the prostate brachytherapy procedure, neither of these is to be touched, yet this is difficult not to do because of the constrained area.

We focus on the needle as the delivery instrument. For many needle insertions, it is vital that the physician have detailed control of the needle position and velocity, since the area surrounding the target location can be easily damaged. Complicating factors include tissue deformation before puncture, needle bending, relaxation of the tissue after puncture, and reduced tactile and visual information. These procedures require rapid reaction time and control greater than typical human ability. However, there exist some

cues that can assist the physician. The amount of force necessary to pierce and travel through different layers of tissue varies based on the material (skin, muscle, fluid, ligament, etc.). Forces also change with needle depth and angle of insertion.

The use of cooperative robotic systems for positioning and manipulating therapy delivery devices presents the option of simultaneous human and computer control. For a method that involves a tool being held or moved by an operator, many factors, such as amount of force applied, are dependent on operator skill. Therefore, operator skill and endurance can affect the results of needle insertion. An important justification for utilizing a robot for assistance during needle insertions is the ability to maintain a controlled velocity behind the needle and react to minute changes in force, which a human user is often unable to do. Clearly, a force sensor is thus required between the robot and the needle to allow the force to be measured. While the physician cannot directly feel interaction forces, information from the sensor can be transmitted through the robot. The computer controlling the robot can determine what speed to move the needle based on real-time force feedback and knowledge of the needle's position. In addition, the surgeon can request that the robot apply virtual fixtures to assist or guide in task execution. Such a system is necessary to assist the surgeon in performing manipulations that demand superior reactions to sudden changes in forces without diminishing their situational awareness. The primary goal of this work is to develop haptic models of percutaneous therapies that can be used to provide appropriate robotic assistance.

Reality-based models, which are developed from measurements of actual tissues, can be used for automatic monitoring of progress and event detection in both freehand and robot-assisted procedures. Refer to Figure 1. Instrumented tools or cooperative robots can enhance the human ability to recognize events during needle insertion by providing additional visual, aural, or haptic feedback. The work discussed in this thesis will demonstrate reality-based models that can provide real-time haptic feedback with cooperative surgical robots, thereby greatly improving accuracy, consistency, therapy delivery speed, and reduction of patient discomfort.

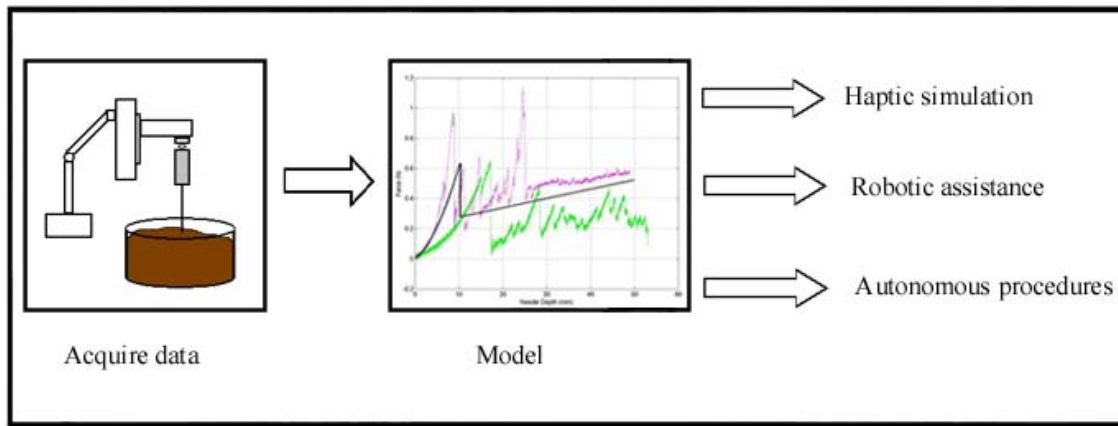


**Figure 1. Data is acquired with a robotic system and used to create reality-based models for later use in haptic simulation, robotic assistance, or autonomous procedures.**

The liver was chosen as the initial organ with which to obtain data. The American Cancer Society estimates that 16,600 new cases (11,000 in men and 5,600 in women) of primary liver cancer and intrahepatic bile duct cancer will be diagnosed in the United States during 2002 [22]. Liver biopsy is a percutaneous procedure that is often used to diagnose the cause of chronic liver disease. It is also used to diagnose liver tumors identified by imaging tests. In many cases a biopsy is used to confirm chronic liver disease, as well as determine the amount of damage to the organ. Liver biopsy is also

used after liver transplantation to determine the cause of elevated liver tests and determine if rejection is present [12]. One approach to treating liver cancer is via ablation. Ablation refers to methods that destroy the tumor without removing it, and is also a percutaneous procedure.

Additionally, an experiment has been performed on the prostate. According to the National Cancer Institute, prostate cancer is the number one incident cancer and the number two cause of cancer deaths among US men. Prostate cancer is a major public health problem, which over a lifetime will affect an estimated one in five American men [19]. One type of treatment for prostate cancer is brachytherapy, another percutaneous procedure in which there is little tactile feedback.

## **1.2 General Background**

To date, a number of researchers have explored ways to improve surgeons' skills in procedures where little visual and direct tactile feedback exists. These mainly take the form of haptic simulators, for procedures such as catheter insertion [7], lumbar puncture [8], epidural blocks [2] [11], endoscopic surgeries [21], and laparoscopic surgeries [17]. While most of the previous work has focused on improving clinical therapies through training, the goal of this research is to develop models that can be used in real-time robotic assistance.

In the areas of telemanipulation and human-robot cooperation, there are a few examples of reality-based modeling used in medical procedures. Yen, *et al.* [23] describe a telemanipulation system for assisting in the penetration of soft tissue for medical tasks. The system interacts with the environment through a rotating arm that performs needle

insertion. They construct a simulation using velocity and acceleration information calculated from encoder readings of a single test of a porcine sample. Brett, *et al.* [1] present an automated handheld device to interpret the type and deformation of tissue while being inserted into recently deceased porcine and human lumbar samples. Components measured include syringe pressure, force, and needle displacement. The instrument's movements are not restricted but rely solely on the surgeon for direction. There has also been recent work in the area of surgical devices to acquire *in vivo* data [3,16].

The cooperative manipulation system used in this work is the Johns Hopkins University Steady-Hand Robot (SHR). This surgical assistance system allows for interactive cooperation between machines and physicians, augmenting human capabilities to achieve manipulation with the precision and sensitivity of a machine, but the manipulative transparency and accessibility of hand-held instruments [20]. Minimally invasive procedures involve conditions of significant sensitivity, and would especially benefit from such systems. In order to effectively use the assistive capabilities of the SHR, real time data must be compared with models and appropriate, contextual assistance provided.

### **1.3 Thesis Contributions**

This thesis describes:

- A method of data acquisition of needle insertion forces such that the stiffness, friction and cutting forces can be identified.

- The modeling and separation of insertion forces into components based upon relative motion of the needle and organ. This division of forces from actual tissue data has not been done previously.

The protocol presented here serves as a general guide for analyzing data from soft tissue needle insertions to create models for eventual use in robot-assisted needle insertions. The initial results show promise for application in large-scale computer integrated surgical systems.

## **1.4 Organization**

The first section of this thesis provides background information about percutaneous therapies and robot-assisted systems. Chapter 2 describes the pre-existing and newly designed equipment used in the experiments. Chapter 3 details the procedures followed in the liver experiments. Chapter 4 discusses the data analysis and modeling from the above experiments. Chapter 5 discusses an experiment performed on a canine cadaver prostate. Chapter 6 presents conclusions and future work. The appendices provide mechanical drawings, data sheets, and CT Fluoro images.

## 2 Experimental Equipment

### 2.1 Steady-Hand Robot

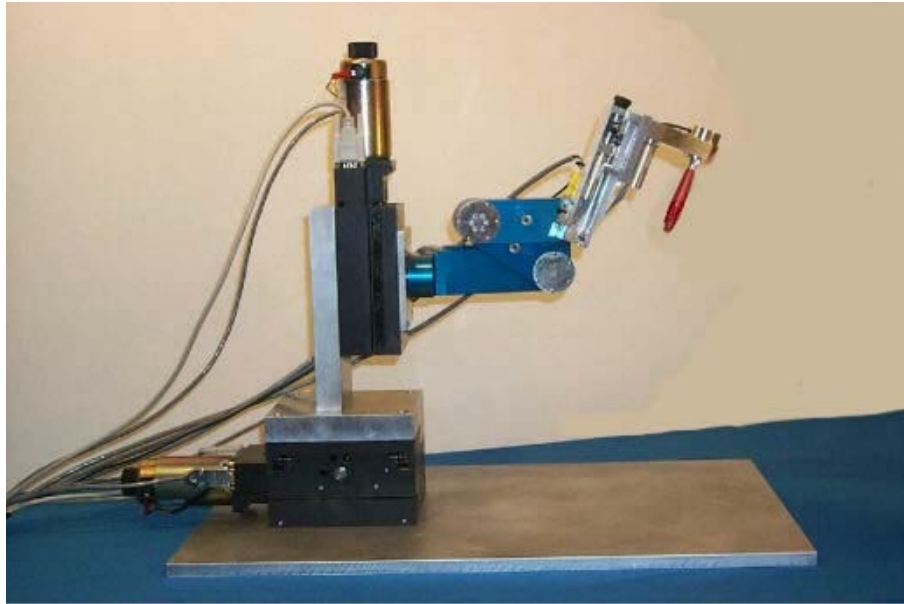


**Figure 2.** The Johns Hopkins University Steady-Hand Robot.

The experimental environment makes use of the insertion stage of the Johns Hopkins Steady-Hand Robot to perform one-dimensional translational motion. This robot (pictured in Figure 2) is a 7-degree-of-freedom manipulator, known for its remote center of motion capabilities, and has a positioning resolution of  $<2.5 \mu\text{m}$  (1.5  $\mu\text{m}$  encoder resolution). In these experiments however, only the motion of the instrument insertion translation stage (Axis 5) is employed. The insertion axis provides translational motion along the instrument tool axis. This axis makes use of a telescoping crossed-roller slide mechanism driven via flexible cable, which provides greater than 150 mm of travel while maintaining high stiffness. During the course of testing, a positional inaccuracy was

found in the configuration file for the 5<sup>th</sup> axis of the Homewood Steady-Hand Robot. It was incorrectly calibrated, with the ratio of actual to programmed displacement of approximately 2:1. The axis was accordingly recalibrated. This positional inaccuracy did not exist with a similar robot used at the Johns Hopkins Medical Institutions (JHMI). In experiments performed at JHMI under CT Fluoro imaging, a separate robot insertion stage, mounted on a passive robot arm, was connected to the controller of a robot at JHMI (CART Robot) instead of utilizing the whole Steady-Hand Robot. The gain values for the insertion stage were found to vary depending on which controller is used. Working values for the two systems can be found in Table 1.

**Table 1. PID gains for each of the robot controllers.**

Gains	Homewood Steady-Hand Robot controller	JHMI CART Robot controller
K <sub>P</sub>	-40	90
K <sub>I</sub>	-1	1
K <sub>D</sub>	-32000	32000

## 2.2 Needle Fixture

The design goals for a needle fixture include the ability to accommodate various sizes of needle hubs, be lightweight, hold the needle firmly without slipping, and interface with the force sensor and the insertion stage of the Steady-Hand Robot. Several designs were considered. The final design is now described.

The needle holder is comprised of a vise grip and several pieces of delrin for the casing (Figure 3). Mechanical drawings of each component may be found in Appendix A.

The design is such that the needle is first inserted into the vise grip and tightened to prevent any travel along its axis. The vise grip is then clenched between symmetrically cut pieces of delrin designed to clamp the vise grip and yet leave sufficient space for needle hubs of a range of sizes. The delrin halves (Figure 4) are held together by a set of four screws, washers, and nuts. Another piece of delrin was designed to screw into the top of the pair. This top plate has a dual purpose: to prevent any potential travel of the needle in the case that the vise grip did not hold properly, and to affix a force sensor at its other end. An advantage of this needle fixture design is that only the top plate needs to be redesigned if a different load cell is used. This situation was encountered when the first force sensor tested was not reliable. Both top plates can be seen in Figure 5. Because the delrin is relatively soft, a HeliCoil screw thread insert was used to prevent wearing of the threads.



**Figure 3.** The delrin needle fixture with needle and force sensor.

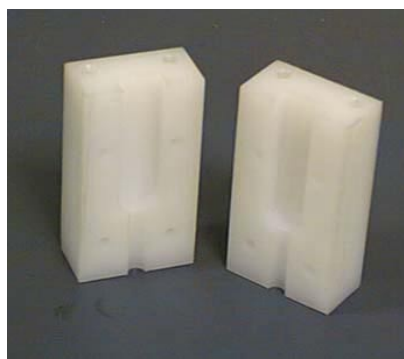


**Figure 4.** Delrin halves of the needle fixture.



**Figure 5 (a)** Top plate for Bokam sensor.

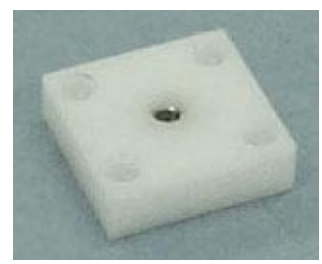


**Figure 5 (b)** Top plate for Entran sensor with HeliCoil insert.

## 2.3 Force Sensor Mounting Flange



Figure 6. The force sensor mounting flange.

An aluminum flange (Figure 6) was produced to interface with the insertion stage of the Steady-Hand Robot and the force sensor attached to the delrin needle holder. A new disc was designed and produced to accommodate the new sensor as well. The six holes around the perimeter of the disc accommodate screws for mounting to the robot, and the tapped center hole accommodates the threaded force sensor. Mechanical drawings can be found in Appendix A.

## 2.4 Force Sensor

A force sensor is necessary to capture the needle insertion forces along the axis of the needle. The first load cell used was a commercially available 3-axis sensor from BOKAM™ (\$349.00), pictured in Figure 7. The operating force is 11.2 N along the X- and Y-axes, and 31.14 N along the Z-axis. The maximum force is 22.24 N along the X- and Y-axes, and 66.72 N along the Z-axis. Only the z-axis was used since the forces felt by a needle upon insertion are primarily along the needle's axis [2]. However, due to a number of problems experienced with this sensor – the presence of high noise levels, hysteresis, and necessary adjustment



Figure 7. Two BOKAM™ force sensors.

of the offset and gains, leading to the maxing-out of potentiometers – another sensor was chosen.

The second force sensor is a small, commercially available 1-axis sensor from Entran™ (\$432.00), pictured in Figure 8. The load cell (model: ELFS-T3E-10N) utilizes micro-miniature semiconductor strain sensing elements for unamplified output signals of 100 mV full scale. It is a 10 N capacity load cell with a sensitivity of 12.3 mV/N, and an overrange limit of 20 N. The sensor is 12.7 mm in diameter, 2.54 mm in height with 9.5 mm threaded mounting studs on each side, and weighs 3.5 grams. The sensor mounts to an aluminum flange attaching it to the instrument rotation stage end-effector with its Z-axis parallel to the instrument insertion stage of the robot. In order to prevent the sensor from being over-torqued, a nut was screwed onto each end and used to tighten the connections to the needle fixture and robot. The analog voltage output from the load cell is converted to digital signals with a National Instruments data acquisition card (Lab-PC+). Due to a slow sampling time (60 Hz) of the amplifier provided by Entran (model: MM50S001U), the analog output curves were stepped. To eliminate this problem, a low noise, low distortion instrumentation amplifier circuit was built using a BURR BROWN® amplifier chip (model: INA103). Data sheets for the chip may be found in Appendix B. The circuit diagram can be seen in Figure 9.



**Figure 8. The Entran™ force sensor.**

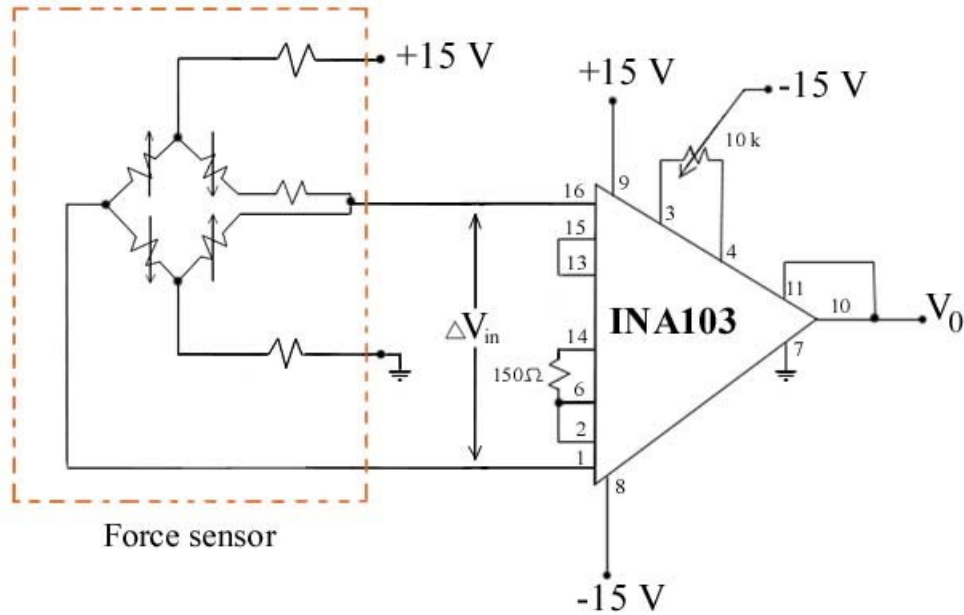


**Figure 9. Circuit diagram for connections from the load cell output to the amplifier circuit and power supply.**

For calibration of the force sensor, we solve an equation of the form  $V = dm + c$ , where  $V$  is the analog output voltage from the load cell,  $m$  is the mass used to obtain the output voltage, and  $c$  and  $d$  are the unknown coefficient variables (the intercept and slope of the linear fit, respectively). The force sensor was loaded from 0 to 850 g in 25 g increments to obtain respective voltage outputs. Data was recorded for 2 seconds. Matrices are then set up in the following standard form

$$\begin{bmatrix} 1 & m_1 \\ 1 & m_2 \\ \vdots & \vdots \\ 1 & m_n \end{bmatrix} \begin{bmatrix} c \\ d \end{bmatrix} = \begin{bmatrix} v_1 \\ v_2 \\ \vdots \\ v_m \end{bmatrix}, \quad (1)$$

so that we have a system of the form

$$A\vec{x} = \vec{v}. \quad (2)$$

Solving for  $\vec{x}$

$$A^T A \bar{x} = A^T \vec{v} \quad (3)$$

$$\bar{x} = (A^T A)^{-1} A^T \vec{v} \quad (4)$$

so that we now have values for  $c$  and  $d$  that fit the equation according to

$$A\bar{x} = \vec{p} = A(A^T A)^{-1} A^T \vec{v} \quad (5)$$

The actual force is then calculated according to

$$F = \frac{(V - V_0) * g}{1000 \frac{g}{kg} * d}, \quad (6)$$

where  $V$  is the measured voltage,  $V_0$  is the initial voltage,  $g$  is the gravitational acceleration, and  $d$  is the slope of the calibration curve for the force sensor in units of Volts/gram.

## 2.5 Friction Experiment Platform

The design goals for a platform for friction experiments include limiting pre-sliding displacement of the liver and maintaining a constant thickness of tissue while the needle is in motion. To realize this, an adjustable-height platform was designed and constructed in such a way that a needle is allowed to pass completely through a lobe of liver while constraining the deflection of the tissue as the needle inserts and withdraws. The structure can be seen in Figure 10a.

The platform consists of a raised acrylic plate with an appropriately placed 3/8-inch diameter hole to accommodate a needle, which fits into the sides of a wooden base. In order to maintain a constant thickness of tissue while the needle is repeatedly passed through it, a second, smaller acrylic plate with a concentric hole for the needle is held above the liver in order to constrain the pull of the tissue in the direction of needle

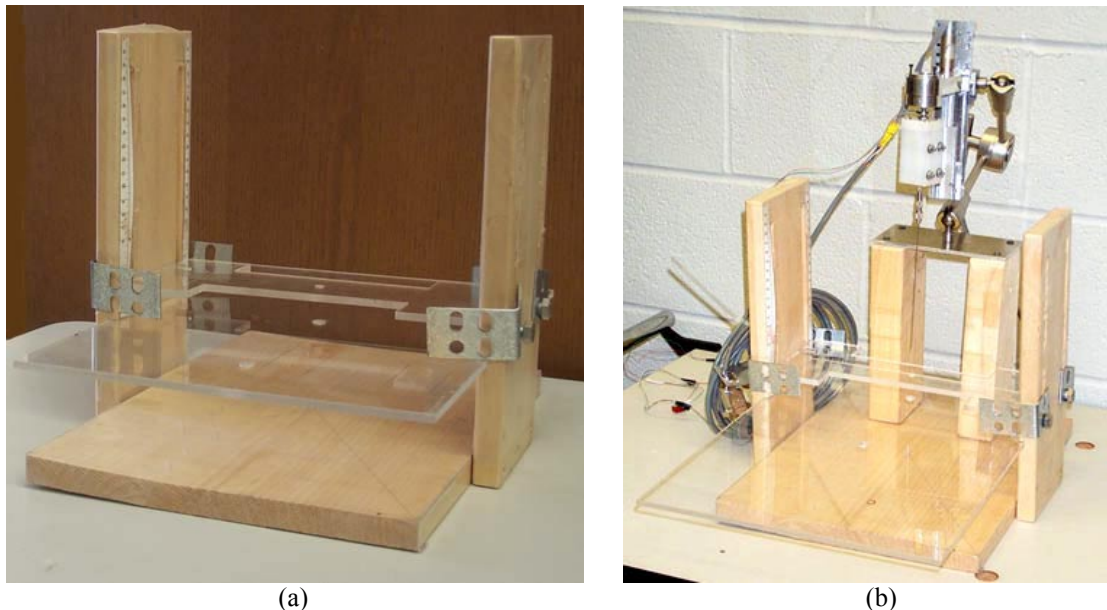


**Figure 10. (a) Original friction experiment platform. (b) Friction experiment platform after modifications for the CT Fluoro experiment.**

motion. The height of this platform is designed to be adjustable to accommodate different thicknesses of liver. To measure the thickness of liver, paper rulers were attached to the sides. For cleanliness, the structure was coated in clear contact paper that could be easily wiped down after experiments. For the CT Fluoro experiment, a slight modification was made to the platform to accommodate the insertion stage attached to a passive arm (Figure 10b). The modification consisted of two 8  $\frac{1}{2}$  -inch high blocks of wood added to the base for the passive arm to attach to, and the large acrylic plate was shifted with a new hole added for the needle.

## 2.6 Control Software

The computer controller consists of a host computer, motor amplifiers, motion control card, power and safety systems, and the necessary connection equipment. The control software executes on a Microsoft Windows NT Pentium II 450 MHz computer.

The software for running the insertion stage of the Steady-Hand Robot was written using Microsoft Foundation Classes in Visual C++ to develop a graphical user interface, or GUI (shown in Figure 11), which enables the user to move the robot in different experimental modes. This software incorporates a modular robot control (MRC) library of C++ classes that has been developed for control purposes by Dr. Rajesh Kumar and Dr. Andrew Bzostek [14]. The library provides Cartesian level control, including classes for kinematics, joint level control, command and command table management, sensor and peripheral support, and network support. The structure of MRC allows the same software to control different robots by simply using the appropriate configuration files.

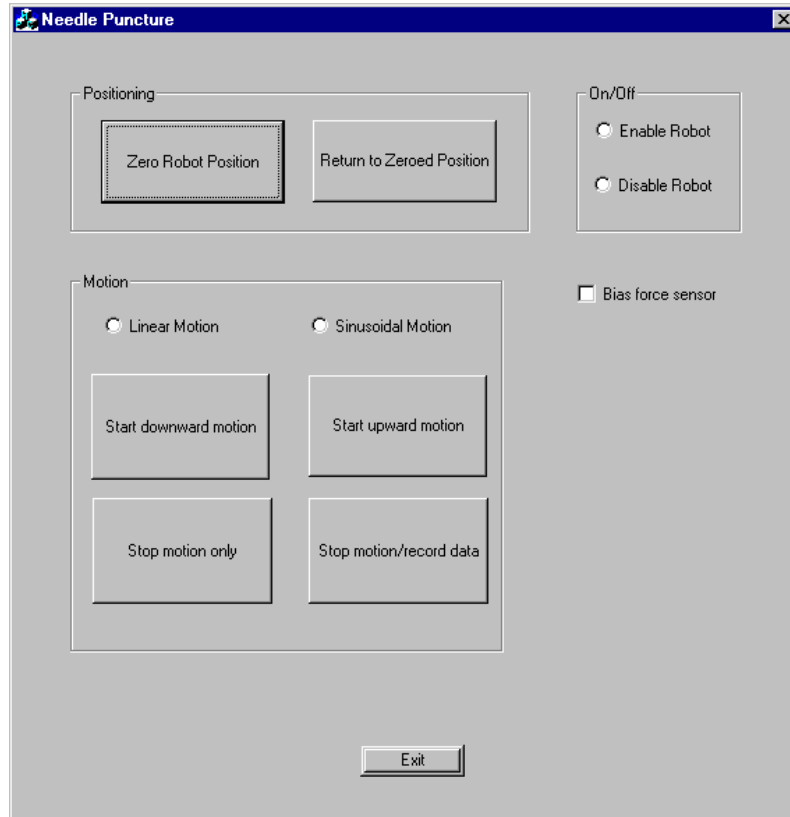


**Figure 11.** The graphical user interface developed for the experiments.

It is desirable to run the data collection at as fast a rate as possible in order to capture sudden changes in forces. A good rate for these experiments is 1 kHz because the puncture phenomena we want to capture occur at a slower rate. After trying a number of system timers, a high-resolution performance counter and multimedia timer was selected and implemented. Although a frequency of 1 kHz was set, some function calls were occupying too much time, resulting in data being recorded at a slower rate. Setting the priority class to “high” for the process had no effect on the time increments. After changing calls to functions for data acquisition so that processing would take less time, a rate of approximately 1 kHz was obtained. Instead of using this inconsistent rate, it was decided to go with the steady rate of 500 Hz since the puncture phenomena can still be adequately captured at this rate.

For one to operate the program, the following sequence on the GUI should be followed: First enable the robot, bias the force sensor, then hit the “Zero Robot Position” button to set the start position at zero. Choose either the linear or sinusoidal radio button depending on the type of experiment being done. The “Start downward motion” button initiates downward motion and starts recording data. The “Start upward motion” button does not initiate data recording and so should not be used to commence motion. The “Stop motion/record data” button should be used at the end of an experiment only since it closes the data files. The “Stop motion only” button should only be used if motion is desired to be stopped during an experiment while still recording data. A safety precaution is incorporated into the code to immediately stop motion if a pre-specified maximum force is reached. Such a situation would exist in surgery if the needle mistakenly contacted bone.

### 3 Liver Experiments

A number of experiments were designed and performed in an effort to model the forces seen by a needle as it passes through tissue. Since there are several forces acting on the needle, it is important to model each force individually and combine them into one model. These forces can be described as the stiffness force of the entire organ before puncture occurs, friction force, and the force required to cut through the internal tissue. The total force experienced by the needle is then the sum of these forces, as represented in the following equation.

$$f_{needle}(x) = f_{stiffness}(x) + f_{friction}(x) + f_{cutting}(x) \quad (7)$$

Experiments were carried out in such a way as to identify specific components of force. Needles with two types of tips (beveled and diamond) were used in these experiments.

#### 3.1 Overall Stiffness

The objective of these experiments was to determine “average” stiffness parameters for a liver. Because the stiffness force is due to the elastic properties of the organ and its capsule, the elasticity of the tissue may be identified from pre-puncture forces in the insertion data.

##### *Procedure:*

These experiments made use of all of the equipment discussed in Chapter 2, except for the friction experiment platform. The setup is pictured in Figure 12. In these experiments, a whole bovine liver was used in order to obtain data that closely corresponds to an intraoperative procedure. The liver was placed into a plastic container to constrain it for



**Figure 12.** The data acquisition system was comprised of the JHU Steady-Hand Robot, a needle holder with load cell, and a control computer.

data acquisition, and occasionally bathed in a normal saline solution to preserve moisture. A beveled needle was inserted at a constant velocity of 4 mm/s within approximately a 15 cm<sup>2</sup> area over the surface of liver 1 and approximately an 8 cm<sup>2</sup> area over the surface of liver 2. This velocity is representative of the speed at which a doctor would insert a needle. 21 data sets were obtained from liver 1, and 14 were obtained from liver 2.

### **3.2 Internal Stiffness / Cutting**

The objective of this experiment was to determine the stiffness properties of the liver tissue that a needle experiences without the effect of the outer capsule.



**Figure 13. The capsule of the liver being removed from the surface.**

*Procedure:*

These experiments made use of all of the equipment discussed in Chapter 2, except for the friction experiment platform. The setup is the same as that in Figure 12. A whole bovine liver was used in order to obtain data that closely corresponds to an intraoperative procedure. The liver was placed into a plastic container to constrain it for data acquisition, and occasionally bathed in a normal saline solution to preserve moisture. The only difference is that the capsule of the liver is first cut away (Figure 13), and a blunt needle is used to prevent the tissue from being cut before obtaining an adequate stiffness curve, since the internal liver tissue is extremely soft and a sharp needle would cut through it much sooner. The needle was inserted at a constant velocity of 2.5 mm/s within approximately a  $6 \text{ cm}^2$  area over the surface. Four data sets were taken with liver 2, but the quality of the data was not good due to excessive noise. Seven data sets were obtained with liver 7.

### 3.3 Friction and Damping

In order to properly identify the friction and damping coefficients, it is necessary to use periodic force data obtained by a needle moving with periodic velocity through a known depth of tissue. Repeated sinusoidal motion along the same vertical line prevents cutting of new tissue, resulting in force measurements due to friction and inertia alone.

*Procedure:*

These experiments made use of all of the equipment discussed in Chapter 2. The use of the friction platform limits the pre-sliding displacement of the liver while maintaining a constant thickness of tissue while the needle inserts and withdraws. The setup is pictured in Figure 14.

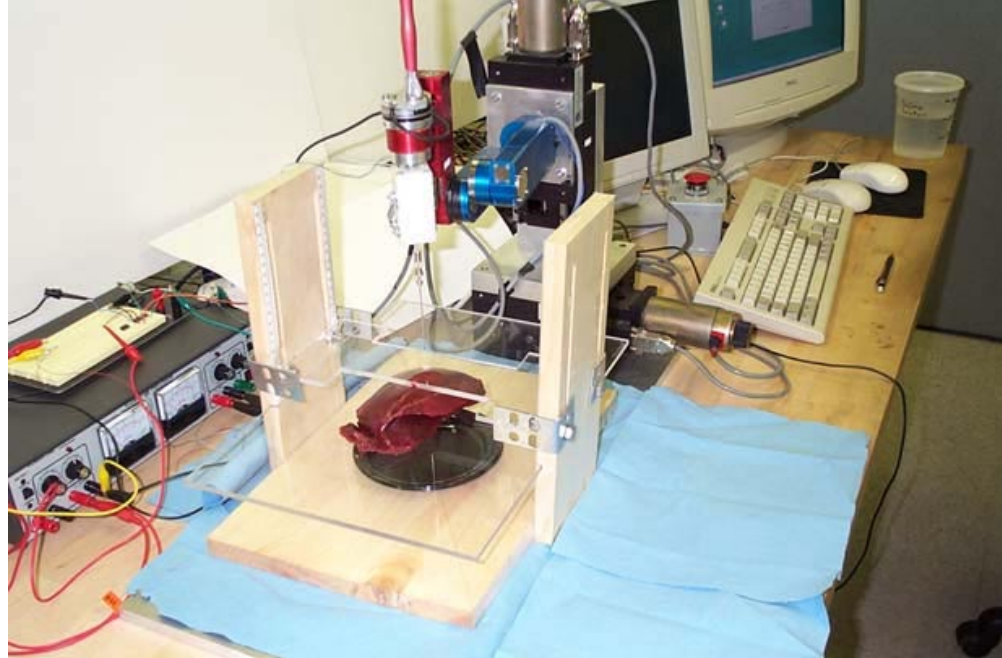


**Figure 14. Friction experiment setup with the Steady-Hand Robot.**

One negative aspect to this method of constraining the liver motion is that the liver is slightly compressed between the plates and only a segment of the organ is tested. However, several preliminary constant velocity insertions without these constraints were performed and it was observed that the force measurements were comparable to the unconstrained liver.

In these experiments, a 258 g piece of an adult steer liver was used due to space constraints of the platform. The lobe of liver was placed over the hole in the bottom acrylic plate of the platform and the second plate positioned above it. The liver thickness was recorded for each insertion. A beveled needle was first passed completely through the lobe so that there is a constant amount of tissue in contact with the needle at any given time (Figure 15). The robot was programmed to move the needle at frequencies of

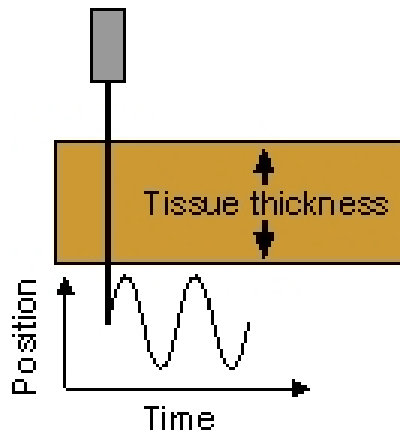


**Figure 15. Graphical representation of the sinusoidal motion of the needle during friction experiments.**

0.2, 0.5, and 0.8 Hz for 7-10 cycles. Data sets for each frequency were taken at seven different locations in the 3<sup>rd</sup> liver.

### 3.4 Stiffness Under CT Fluoro Imaging

The objective of these experiments was to determine an “average” stiffness parameter for a liver in the same way as described in Chapter 3.1, but while under fluoroscopic imaging so that the deformation of the tissue can be noted. A preliminary experiment with a 575 g lamb liver determined that artifacts resulting from the metal in the setup would not interfere with the ability to obtain usable images under fluoroscopy with the CT Fluoro machine.

One limitation in using CT Fluoro imaging lies in the way that it forms final images. The Toshiba Aquilion CT Fluoro™ machine acquires four simultaneous 0.5 mm slices in every  $\frac{1}{2}$ -second rotation of the gantry. These four slices are converted into three simultaneous images on the display. One image represents the slice just before the target,

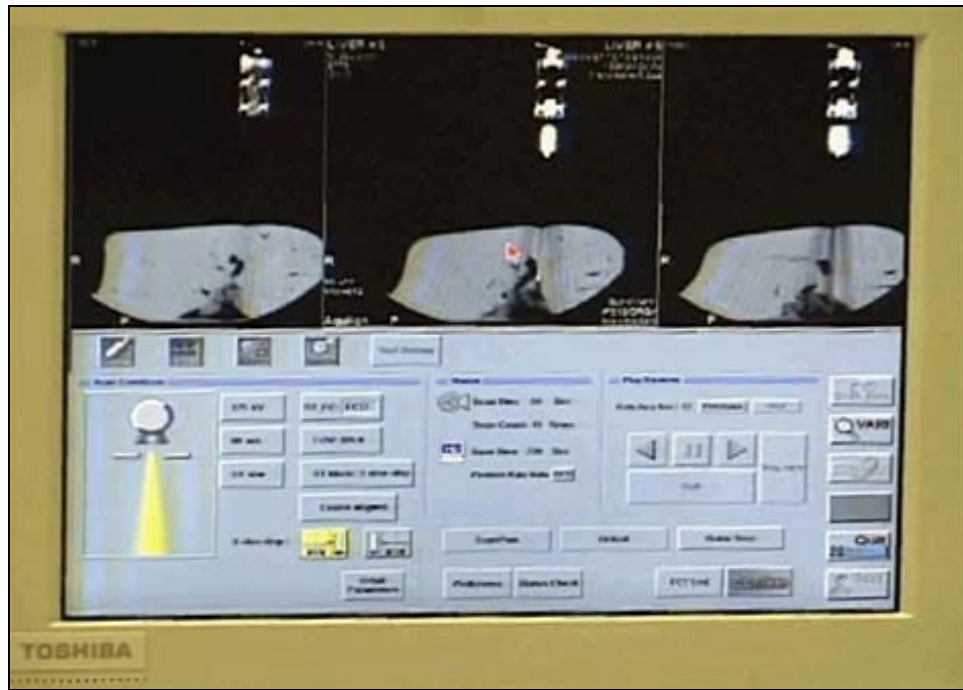


Figure 16. An image of the CT Fluoro console during a typical needle insertion (taken from digital video recordings).

one is the slice right after the target, and one image combines two slices for a high-resolution view of the target [15]. Because the diameter of the needle is small, it is usually only visible in the combined center image. A typical view of the screen can be found in Figure 16. Thus, when imaging is complete, the needle is less able to be seen. Another limitation in using CT Fluoro is that in general, it is not sensitive enough to pick up fine tissue details, only some major blood vessels in the viewing field. The contrast of the view must be adjusted to minimize the presence of artifacts from the metal in the slice, which also limits the detail of the tissue. However, it is sufficient because the tissue and needle motion are easily viewed, and is the best imaging technology available for these types of experiments.

*Procedure:*

This experiment made use of all of the equipment discussed in Chapter 2, except for the friction experiment platform. This experiment was performed at the Johns Hopkins Medical Institutions, using a clinical Toshiba Multi-Slice Aquilion 0.5 CT Fluoro<sup>TM</sup> machine. The setup is pictured in Figure 17.

In this experiment, a whole bovine liver was used in order to obtain data that closely corresponds to an intraoperative procedure. The liver was placed into a plastic container to constrain it for data acquisition, and occasionally bathed in a normal saline solution to preserve moisture. A separate insertion stage was mounted to a passive arm. A diamond tip needle was inserted at a constant velocity of 4 mm/s within approximately a 15 cm<sup>2</sup> area over the surface. During each insertion, digital videos of the imaging monitor

were recorded, showing each of the slices. Imaging data was acquired at a rate of 29.97 frames per second (standard NTSC rate). 11 data sets were obtained from liver 5.



**Figure 17. Stiffness experiments under CT Fluoro imaging.**

### **3.5 Friction and Damping Under CT Fluoro Imaging**

The objective of this experiment was to obtain friction data while under fluoroscopic imaging using a CT Fluoro machine. Imaging permits the measurement of the relative velocities of the tissue and needle, allowing the use of a more complete model for friction that includes pre-sliding displacement, such as required for a bristle or Dahl friction model [10]. Such a model will likely give more consistent results, as tissue deformation clearly occurs prior to relative motion between the needle and tissue.

*Procedure:*

These experiments made use of all of the equipment discussed in Chapter 2. The platform used was modified from the original version, as explained in Chapter 2.5. The use of the friction platform limits the pre-sliding displacement of the liver while maintaining a constant thickness of tissue while the needle inserts and withdraws. The general setup is pictured in Figure 18, while a close-up is shown in Figure 19.



**Figure 18. The setup for friction experiments under CT Fluoro imaging.**

In these experiments, a 690.5 g piece of an adult steer liver was used due to space constraints of the platform. The lobe of liver was placed over the hole in the bottom acrylic plate of the platform and the second plate positioned above it. The liver thickness was recorded for each insertion. A diamond tip needle was first passed completely through the lobe so that there is always a constant amount of tissue in contact with the needle at any given time (see Figure 15 from the previous section). The robot was

programmed to move the needle at frequencies of 0.2, 0.5, and 0.8 Hz for 7-10 cycles.

Data sets for each frequency were taken at five different locations in the 7<sup>th</sup> liver.



**Figure 19. Friction setup in the CT Fluoro machine.**

## 4 Data Analysis for Liver

### 4.1 Property Estimation

In order to model the needle insertion forces accurately, it is necessary to separate the data into its components. To the best of the author's knowledge, there has been no prior work regarding the separation of needle forces into its components for the purposes of modeling. Graphs of the data (Figure 20) reveal two main phases: pre-puncture and post-puncture.

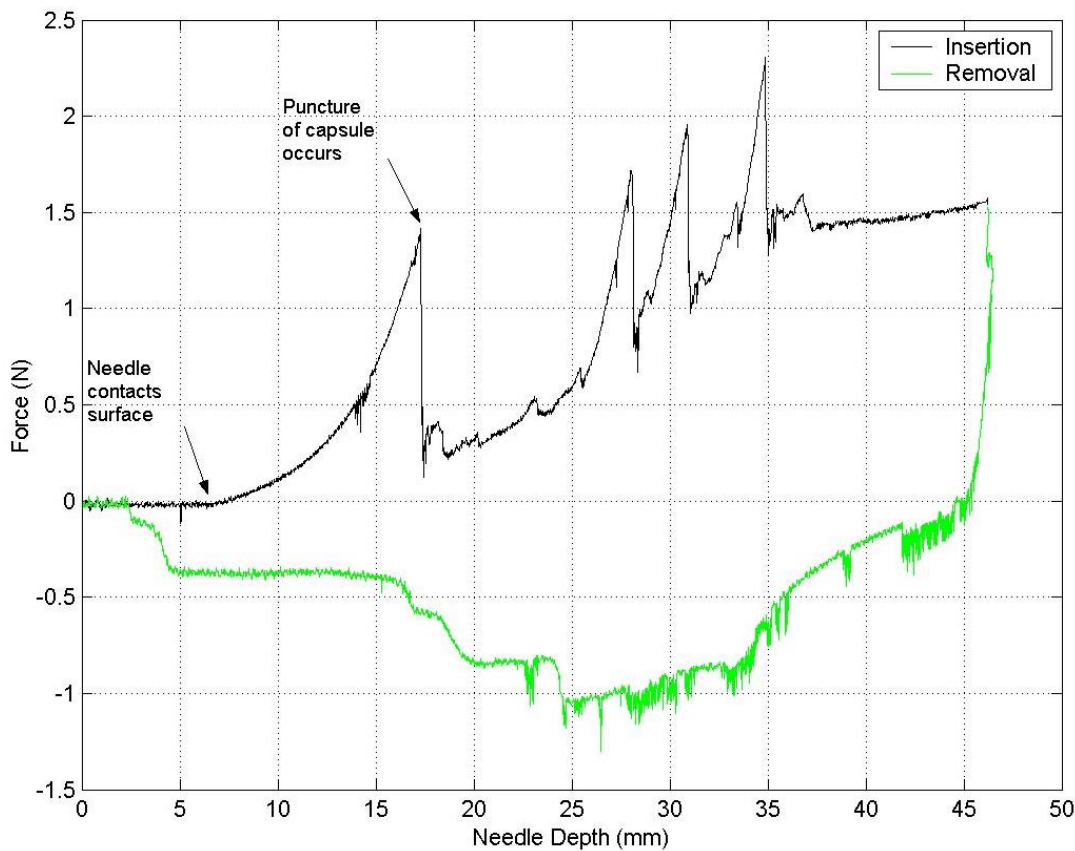
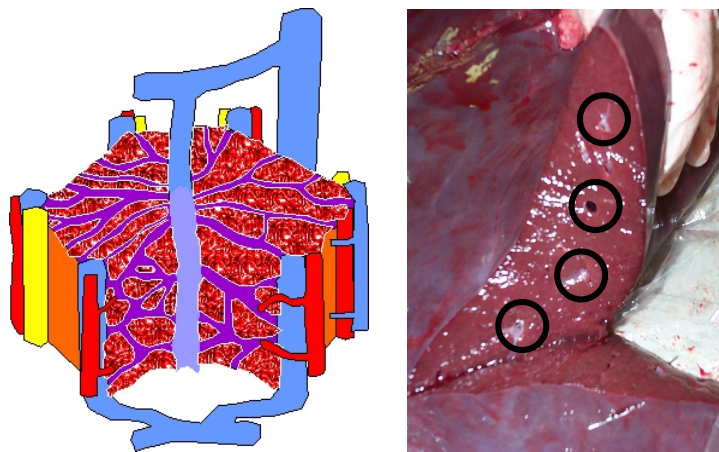


Figure 20. A typical force vs. position plot showing insertion and removal forces, and events such as puncture.

The main puncture event is designated by a peak in force after a steady rise, followed by a sharp decrease. Subsequent variations in force are due to friction, cutting forces/internal stiffness, as well as collisions with and puncture of interior structures. The force data collected is a summation of stiffness, friction, and cutting forces. The stiffness force is pre-puncture, and the friction and cutting forces post-puncture. Cutting forces are considered to include the forces of plastic deformation from slicing through the tissue, which is determined by the puncture force of the liver without its membrane. The total force is thus represented by equation 7, as given in Chapter 3 and repeated below.

$$f_{needle}(x) = f_{stiffness}(x) + f_{friction}(x) + f_{cutting}(x) \quad (8)$$

Before proceeding, it is necessary to note the anatomy of the liver. Because this organ functions to filter and process blood, it contains a substantial number of arteries and veins. The structural and functional units of the liver are ~2mm, hexagonally-shaped lobules which are comprised of liver cells arranged in one-cell-thick plate-like layers that radiate from the central vein to the edge of the lobule (Figure 21).



**Figure 21.** Three-dimensional representation of one liver lobule, which includes many interior structures, (left, adapted from [13]), and a cutaway of one of the livers used in the experiments, revealing large interior vessels (right).

At each of the six corners of a lobule is a portal triad, consisting of a branch of the hepatic artery, hepatic portal vein, and a bile duct [13]. It is for this reason that several puncture events (identified by elevated forces and subsequent sudden drops in force) are noted after the initial penetration in Figure 20.

In analyzing the data, the force values before the needle contacts the surface of the organ were averaged and used to zero the forces.

#### **4.1.1 Stiffness / Puncture**

The stiffness force is due to the elastic properties of the organ and its capsule. The elasticity of the tissue can be identified from pre-puncture forces in the insertion data. Numerous constant velocity insertions at 4 mm/s within a 15 cm<sup>2</sup> area were performed on bovine livers 1, and within an 8 cm<sup>2</sup> area on liver 2. The general form of the force on the needle is described by the relationship

$$f_{stiffness} = \begin{cases} 0 & x_{tip} < x_{s1} \\ f(x) & x_{s1} \leq x_{tip} \leq x_{s2} \\ 0 & x_{tip} > x_{s3} \end{cases}, \quad (9)$$

where  $f(x)$  is a one-dimensional quasi-static stiffness model, and  $x_{tip}$  and  $x_{s1}, x_{s2}, x_{s3}$  are the positions of the needle tip and tissue surface relative to a fixed coordinate system before puncture. The relative locations of  $x_{s1}$ ,  $x_{s2}$ , and  $x_{s3}$  can be seen in Figure 22. All positions are considered to be relative to a fixed coordinate system. The position  $x_{s3}$  is less than  $x_{s2}$  due to relaxation of the tissue after puncture.

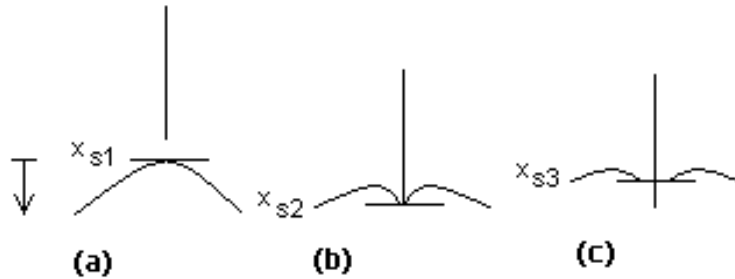


**Figure 22. Locations of the tissue surface at different stages of needle insertion. (a) pre-puncture (b) puncture (c) post-puncture.**

Biological tissue is linearly elastic for small deformations [6]. However, it is clear from the data that there is a large amount of deformation before puncture, so the force must be modeled using a nonlinear method.

In the search for a relation to model the deformation of the tissue, a nonlinear spring model was tested, as demonstrated by d'Aulignac *et al.* [4] in modeling deformation of a human thigh. That relation is given by

$$f(x) = \frac{x}{ax + b}, \quad (10)$$

where  $x$  is the difference in the length of the springs with respect to their original, resting length. The parameters  $a$  and  $b$  were fitted to match the deformation measured on bovine livers. However, lower rms error values were found using several polynomial models. Two methods were then used to find a fit to the data. In the first approach, each run of data was fit individually and the coefficients were averaged to obtain a model. A polynomial up to order 4 was tried, but the highest order was discarded since the change in rms errors of the coefficients was insignificant between those obtained in the next lower order. Modeling with a third order polynomial yielded the coefficient of the highest order term to be close to zero. To compare a second and third order polynomial fit, a

second approach was taken where all data points were fit at once and the respective  $r^2$  values compared. Since the  $r^2$  values were similar, the third order polynomial model was discarded. Therefore, a second order polynomial of the form

$$f(x) = a_0 + a_1x + a_2x^2, \quad (11)$$

best fits the experimental data. The assumption is made that the force is zero before the needle contacts the surface, so in the model, the intercept  $a_0$  is set to zero. Typical stiffness data and a model can be seen in Figure 23.

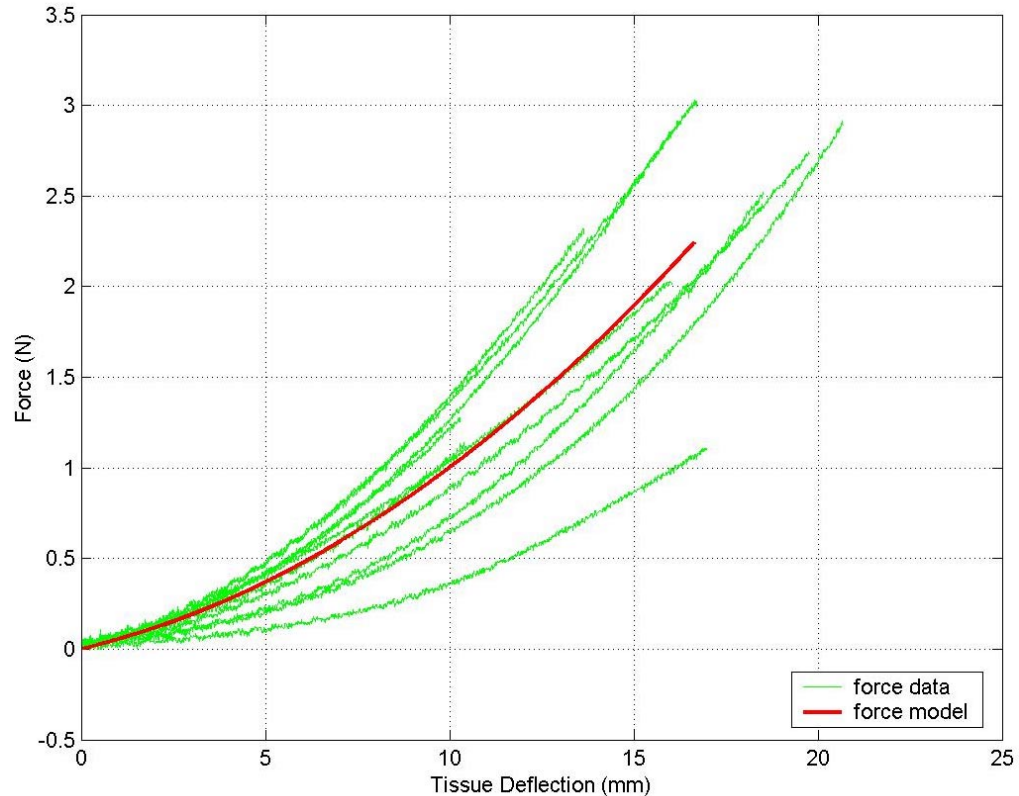


**Figure 23. Typical stiffness data for a bovine liver before membrane puncture within a 10 cm<sup>2</sup> area.**

Fitting all data points at once obtained a slightly different model than averaging a separate fit of each run. The coefficient values from modeling all data at once are presented in Table 2. Also given are the average positions (relative to the liver surface) at

**Table 2. Values of the estimated pre-puncture nonlinear stiffness parameters ( $a_1$ ,  $a_2$ ) for each liver.**

Liver #	Needle tip type	$a_1$ [N/m]	$a_2$ [N/m $^2$ ]	Average puncture position [mm]	Average Puncture force [N]
1	beveled	0.0480	0.0052	16.5732	2.3888
2	beveled	0.0020	0.0023	22.3838	1.2597
3	beveled	0.0371	0.0107	8.9458	1.4370
5	diamond	0.0204	0.0008	10.4022	0.5352
7	diamond	0.0042	0.0133	8.0068	1.1283

which puncture occurred (corresponding to  $x_{s2}$  in Figure 22), and the average puncture forces. Different locations in the liver are likely to have variations in stiffness values due to the presence of internal structures as noted in Figure 21.

It is worthwhile to note that in the one-dimensional insertions into livers 5 and 7, a diamond point needle was used, which resulted in an additional event in the force profiles as compared to those obtained from livers 1, 2, and 3, which were punctured with a beveled Quincke point spinal needle. Both tips are pictured in Figure 24. With the diamond-point needle there is a “pre-puncture” event (visible in Figure 25) that occurs possibly when the sharp sheath catches on the tissue while the point has already punctured the surface.

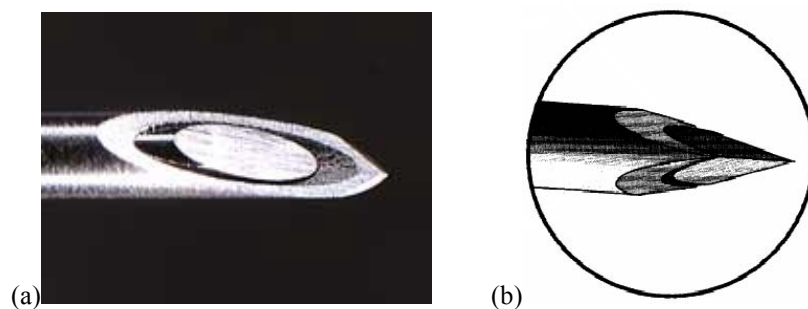


**Figure 24. The two types of needle tips used in experiments. (a) A beveled Quincke point spinal needle. (b) A diamond point needle.**

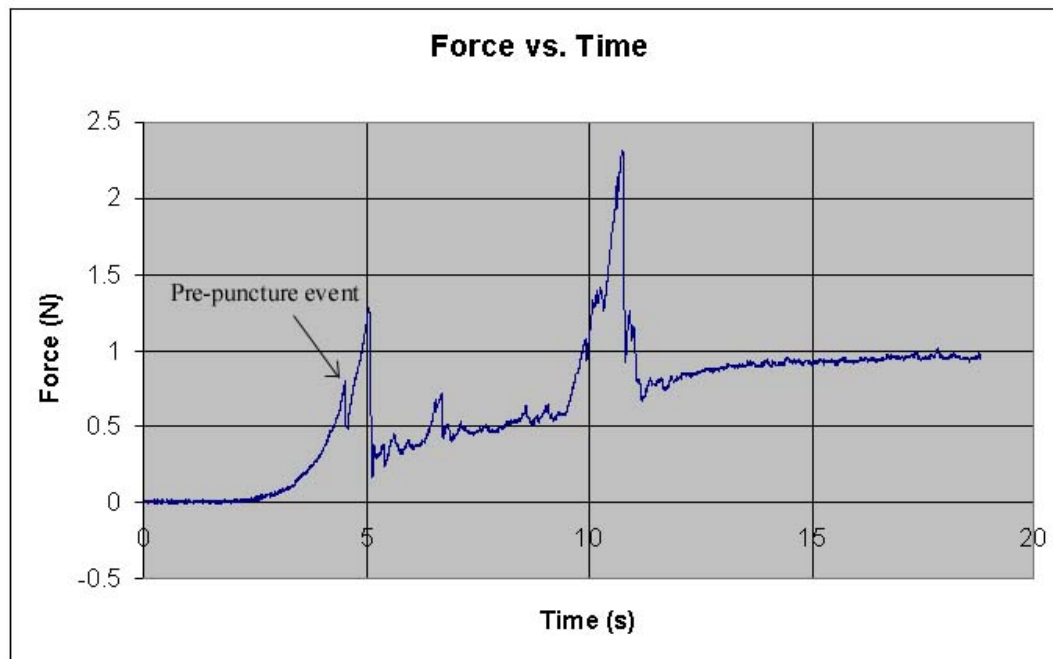


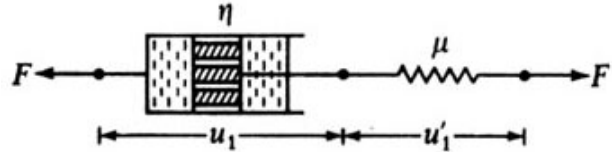
**Figure 25. Typical force data for an insertion into liver with a diamond tip needle. A pre-puncture event is evident.**

In the internal stiffness/cutting experiment, it was found that the force required to puncture the interior tissue is very small. Only a maximum puncture value of 0.243 N was attained with a blunt tip. The average puncture force was found to be 0.0858 N. With a sharp tip, even lower forces would have been able to puncture the tissue. Because this stiffness only applies when the needle is past the outer membrane of the liver, it is not used in the final model. This data could be used in future models however, to account for a needle that has already passed through the capsule and has been withdrawn and repositioned while still in the organ. The puncture value for a sharp tip should correspond to the cutting force. In that case, new internal tissue would still be cut. The estimated coefficient values,  $a_1$  and  $a_2$ , for the second order polynomial model  $f(x) = a_0 + a_1x + a_2x^2$  are presented in Table 3.

**Table 3. Values of the nonlinear stiffness parameters ( $a_1$ ,  $a_2$ ) for internal stiffness measurements.**

Liver #	$a_1$ [N/m]	$a_2$ [N/m <sup>2</sup> ]
7	0.0056	0.0024

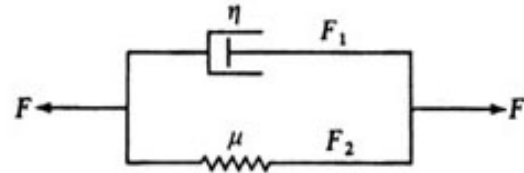
Other models that have been used by other researchers have been investigated as well. While viscoelastic conditions exist in tissues, the linear laws of viscoelasticity put forth by Fung [6] are not appropriate here simply because my force vs. position data was nonlinear. These linear models are shown below:



$$\dot{u} = \frac{\dot{F}}{\mu} + \frac{F}{\eta}$$

$$u(0) = \frac{F(0)}{\mu}$$

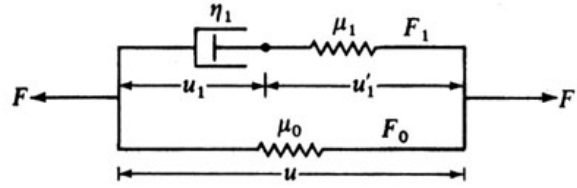
**Figure 26. Maxwell body [Fung, 6]**



$$F = \mu u + \eta \dot{u}$$

$$u(0) = 0$$

**Figure 27. Voigt body. [Fung, 6]**



$$u = u_1 + u'_1$$

$$F = F_0 + F_1$$

$$F_0 = \mu_0 u$$

$$F_1 = \eta_1 \dot{u}_1 = \mu_1 u'_1$$

$$F = \mu_0 u + \mu_1 u'_1$$

$$F = \mu_0 u + \mu_1 (u - u_1)$$

$$F = (\mu_0 + \mu_1) u - \mu_1 u'_1$$

**Figure 28. Kelvin body.** [Fung, 6]

Equations used by Ottensmeyer, et al. [16] and Brouwer, et al. [3], who are developing devices to acquire *in vivo* data were also examined. Ottensmeyer, et al. [16] approximate tissue geometry by a semi-infinite body undergoing normal indentation by a right circular punch as illustrated below

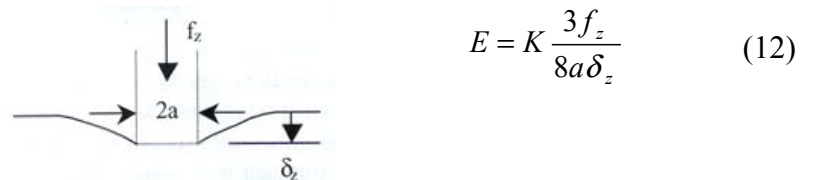


**Figure 29. Indentation of a semi-infinite elastic body with a rigid, right circular punch.**

[Ottensmeyer, 13]

where  $\delta_z$  and  $f_z$  are the displacement and force normal to the surface,  $a$  is the cylindrical indenter radius, and  $E$  is Young's modulus. For a semi-infinite body,  $K$  is unity. Solving for force in equation 12, one obtains:

$$f = \frac{8Ea\delta}{3K}. \quad (13)$$

This relation is inappropriate to the work presented here because they assume constraints that do not match my experimental setup. Not only does their needle have a blunt tip while the ones used in my research have a sharp, beveled or diamond tip, but their boundary conditions assume that the tissue geometry can be approximated by a semi-infinite body with effectively simply-supported end conditions, while in reality the end conditions deform as well.

Brouwer et al. [3] make use of the following exponential function

$$F(\lambda) = \alpha e^{B\lambda}, \text{ where } \lambda = \frac{l}{l_0}. \quad (14)$$

Their experiments however, acquire data from stretching the tissue in a tensile test arrangement, resulting in constraints that also differ from my experimental setup.

#### **4.1.2 Friction / Damping**

The friction force occurs along the length of the needle, and is due to tissue adhesion and damping. A friction model should be simple and not require extremely accurate measurements of velocity at low speeds. This is because of the difficulty in sensing velocity in the experimental setup, since encoders are relied upon for position sensing. For this reason, a Karnopp model was considered. In this model, friction is a function of velocity. When the velocity of the system approaches zero, the velocity is taken to be exactly zero. The width of this band around zero velocity is determined by the velocity value required to maintain the system at zero velocity. All of the model parameters can be expressed as linear coefficients of the independent variables velocity

and acceleration [5]. A graphical representation of the Karnopp model can be seen in Figure 30a.

However, a modified version of the Karnopp friction model (used by Richard, [18], and shown in Figure 30b) is most appropriate to soft tissue data modeling for the following reasons. This representation includes both Coulomb and viscous friction and allows for

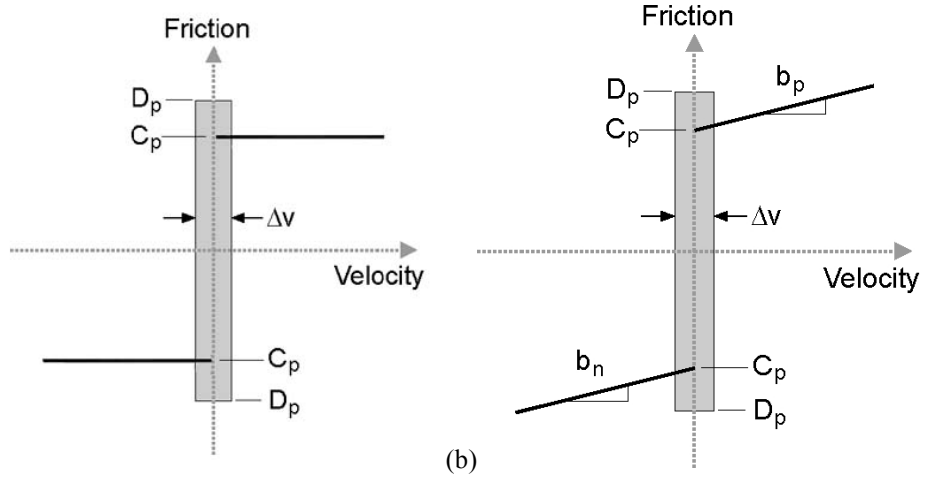


**Figure 30.** (a) The Karnopp friction model (adapted from [18]). (b) The modified Karnopp friction model (adapted from [18]).

asymmetric values for positive and negative velocities. It accounts for the stick-slip friction, or “stiction,” phenomenon by having the static value of friction higher than the dynamic value. The model equation is

$$F_{friction}(\dot{x}, F_a) = \begin{cases} C_n \operatorname{sgn}(\dot{x}) + b_n \dot{x} & \dot{x} \leq -\frac{\Delta v}{2} \\ \max(D_n, F_a) & -\frac{\Delta v}{2} < \dot{x} \leq 0 \\ \min(D_p, F_a) & 0 < \dot{x} < \frac{\Delta v}{2} \\ C_p \operatorname{sgn}(\dot{x}) + b_p \dot{x} & \dot{x} \geq \frac{\Delta v}{2} \end{cases} \quad (15)$$

where  $C_n$  and  $C_p$  are the negative and positive values of dynamic friction,  $b_n$  and  $b_p$  are the negative and positive damping coefficients,  $D_n$  and  $D_p$  are the negative and positive values of static friction,  $\dot{x}$  is the relative velocity between the needle and tissue,  $\frac{\Delta v}{2}$  is the value below which the velocity is considered to be zero, and  $F_a$  is the sum of non-

frictional forces applied to the system (which includes inertial effects and force due to elasticity of the tissue during any pre-sliding displacement of the liver).

In order to properly identify the friction and damping coefficients, force data was obtained by passing a needle completely through one lobe of a liver whose thickness is known so that there is always a constant amount of tissue in contact with the needle at any given time (Figure 15 in Chapter 3.3). A sinusoidal velocity of the needle was chosen to obtain force data at a range of smooth velocities. The procedure for these experiments is outlined in Chapter 3.2. By using the adjustable-height platform described in Chapter 2.5, pre-sliding displacement of the liver was limited and a constant thickness in contact with the needle is attained during motion of a needle with periodic velocity. The robot was programmed to move the needle at amplitudes of 10mm, and frequencies of 0.2, 0.5, and 0.8 Hz for 7-10 cycles. Repeated sinusoidal motion along the same vertical line prevents cutting of new tissue, resulting in force measurements due to friction and inertia alone.

By examining the videos taken of the CT Fluoro console during the friction experiment, different phases of the force profiles can be characterized. In each direction of motion, there are three distinct phases of data (noted in Figures 31 and 32) that correspond to varying relative velocities between the needle and the liver. One phase can be further broken into two subsections. The demarcation of these phases is dictated by the presence of the acrylic plates that sandwich the liver. The phases occur (a) from when the needle and liver are at a maximum position and velocity has just started to be non-zero (position 1 and 5), to when the liver first contacts the plate and the bulk of its mass stops moving because of this constraint (position 2 and 6); (b) from the point where the liver

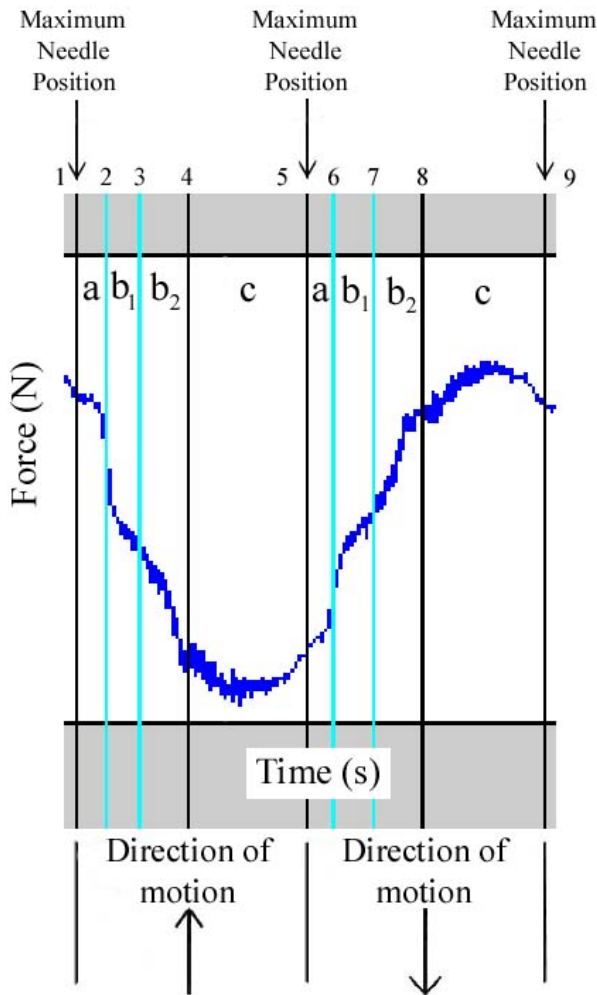


**Figure 31. One period of force versus time data with segments highlighted.**

first contacts the plate while there is still some tissue motion at the hole where the needle is allowed to pass (position 2 and 6), to when the tissue has completely stopped moving and is at its maximum position (position 4 and 8); and (c) from when the tissue has completely stopped at its maximum position (position 4 and 8), to when the needle is at its maximum position (position 5 and 9). Phase b is further segmented into 2 subdivisions. Phase  $b_1$  occurs from the time at which the liver first contacts a plate (position 2 and 6) to when the liver fully contacts the plate (position 3 and 7). Phase  $b_2$  occurs from the time at which the liver fully contacts a plate (position 3 and 7) while

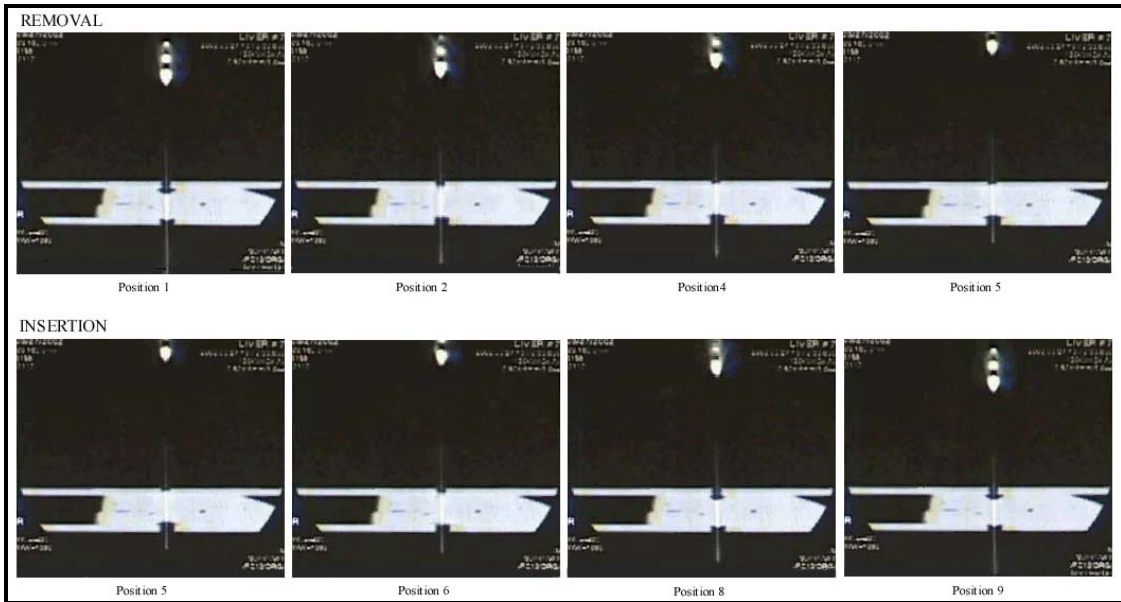


**Figure 32. Images of the CT Fluoro console during a periodic needle insertion into liver. An enlarged version can be found in Appendix C.**

there is still some tissue motion through the hole, to when the tissue has completely stopped moving and is at its maximum position (position 4 and 8). At positions 1, 5, and 9, the needle and liver are at maximum displacements, where the velocities are zero and the accelerations are maximum. At positions 4 and 8, the needle and liver are at zero displacements, where the velocities are maximum and the accelerations are zero. Positions 2, 3, 6 and 7 occur at some location between the zero and maximum displacements.

The relative velocity of the needle in the tissue is represented by the following equation

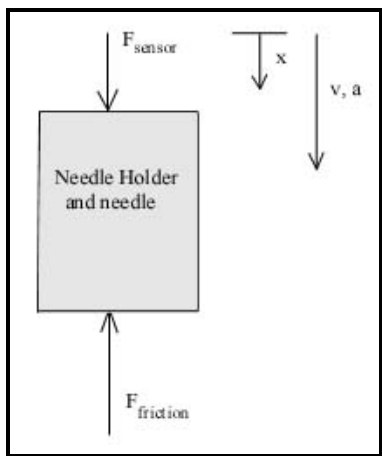
$$v_{relative} = v_{needle} - v_{liver} \quad (16)$$

The needle has a constant velocity of 4 mm/s. In phase a, the static friction predominates the behavior of the system, so the liver and needle move in unison. In this case, the

velocity of the needle equals that of the liver, thus the relative velocity is zero. During phase b, the portion of the liver not constrained by the plate, i.e. at the hole where the needle passes, is still in motion. In this case, the velocity of the liver is smaller than that of the needle, which results in some relative velocity between them, as represented by equation 16. As previously mentioned, phase b is subdivided into 2 parts. During phase  $b_2$ , the relative velocity of the needle in the liver is slightly greater than the relative velocity during phase  $b_1$  due to the constraints of the hole/plate combination. In phase c, the tissue is no longer moving, resulting in the relative velocity equaling that of only the needle, such that phase c is completely dominated by the dynamic friction. For the purposes of modeling, only the portions of data where the relative velocity is known ( $v_{\text{relative}} = 0$  in phase a, and  $v_{\text{relative}} = v_{\text{needle}}$  in phase c) are used to compute the coefficients of static and dynamic friction, respectively.

The data was analyzed using a Matlab<sup>TM</sup> program, adapted from code provided by Richard [18]. The data input to the program includes time, position and force of the needle. The program first smoothes the original position and force data using a moving average filter. The position data was used to calculate velocity and acceleration, which were also both smoothed with a moving average filter. The size of all the data was then reduced by 100 data points on each end to remove any boundary effects. The data must be segmented to model the two types of friction, static and dynamic. To obtain the coefficients of static friction, the portions of data used are those from when the system is at zero velocity to when there has just started to be a relative velocity between the needle and liver. This corresponds to phase a. To determine the coefficients of dynamic friction and damping coefficients, the portions of data used are those in which the relative

velocity between the needle and liver equals the known needle velocity (because the tissue has stopped moving). This corresponds to phase c in Figure 31. Since the velocity is assumed to be zero around a band of 0.005 m/s (determined by the boundary of phase a), any force, velocity, and acceleration data in that interval was removed. For analysis, the rest of the data is separated according to positive and negative velocities. Two approaches were taken to determine the friction parameters. In one, the mass of the needle holder and needle were included in the parameters to be estimated, and in the other, the inertia effect was subtracted out of the sensor data so that the estimated parameters were only for the friction model. Refer to the free-body diagram in Figure 33 for the following governing equations.



$$\sum F_x = ma \quad (17)$$

$$F_{sensor} - F_{friction} = ma \quad (18)$$

$$F_{sensor} = m_{est} a + F_{friction} \quad (19)$$

$$F_{sensor} = ma + F_{friction} \quad (20)$$

$$F_{sensor} - ma = F_{friction} \quad (21)$$

**Figure 33. Free-body diagram of the system.**

$F_{sensor}$  is the force data from the sensor,  $F_{friction}$  is the frictional force of the liver acting to oppose the motion of the needle,  $m$  is the measured mass of the needle holder and needle ( $m = 0.087$  kg), and  $m_{est}$  is the mass of the needle holder and needle as estimated by the program. Equation 19 is used in the first approach, where the sensor data,  $F_{sensor}$ , is used to estimate the terms on the other side of the equality. Equation 21 is used in the second

approach, where the inertia effects are brought to the other side of the equality so that only the friction force,  $F_{friction}$ , is estimated. The two systems of equations, 19 and 21, are solved using linear least squares regression. For equation 19, matrices are set up in the following standard form

$$\begin{bmatrix} a_1 & \text{sgn}(+v_1) & +v_1 & \text{sgn}(-v_1) & -v_1 \\ a_2 & \text{sgn}(+v_2) & +v_2 & \text{sgn}(-v_2) & -v_2 \\ \vdots & \vdots & \vdots & \vdots & \vdots \\ a_m & \text{sgn}(+v_m) & +v_m & \text{sgn}(-v_m) & -v_m \end{bmatrix} \begin{bmatrix} m_{est} \\ c_p \\ b_p \\ c_n \\ b_n \end{bmatrix} = \begin{bmatrix} F_1 \\ F_2 \\ \vdots \\ F_m \end{bmatrix} \quad (22)$$

while for equation 21, matrices are set up as below

$$\begin{bmatrix} \text{sgn}(+v_1) & +v_1 & \text{sgn}(-v_1) & -v_1 \\ \text{sgn}(+v_2) & +v_2 & \text{sgn}(-v_2) & -v_2 \\ \vdots & \vdots & \vdots & \vdots \\ \text{sgn}(+v_m) & +v_m & \text{sgn}(-v_m) & -v_m \end{bmatrix} \begin{bmatrix} c_p \\ b_p \\ c_n \\ b_n \end{bmatrix} = \begin{bmatrix} F_1 \\ F_2 \\ \vdots \\ F_m \end{bmatrix} \quad (23)$$

so that in either case, we have a system of the form

$$A\vec{x} = \vec{f} \quad (24)$$

Solving for  $\vec{x}$

$$A^T A \vec{x} = A^T \vec{f} \quad (25)$$

$$\vec{x} = (A^T A)^{-1} A^T \vec{f} \quad (26)$$

so that we now have values for the parameters  $m_{est}$ ,  $c_p$ ,  $b_p$ ,  $c_n$ , and  $b_n$  that fit equation 19, or  $c_p$ ,  $b_p$ ,  $c_n$ , and  $b_n$  that fit equation 21.

Typical velocity and force data, along with a fit of the friction model, is shown in Figure 34. Figure 35 presents the plots with the three phases highlighted. The values of the coefficients varied somewhat for the different frequencies used, as shown in Tables 4 and 5.

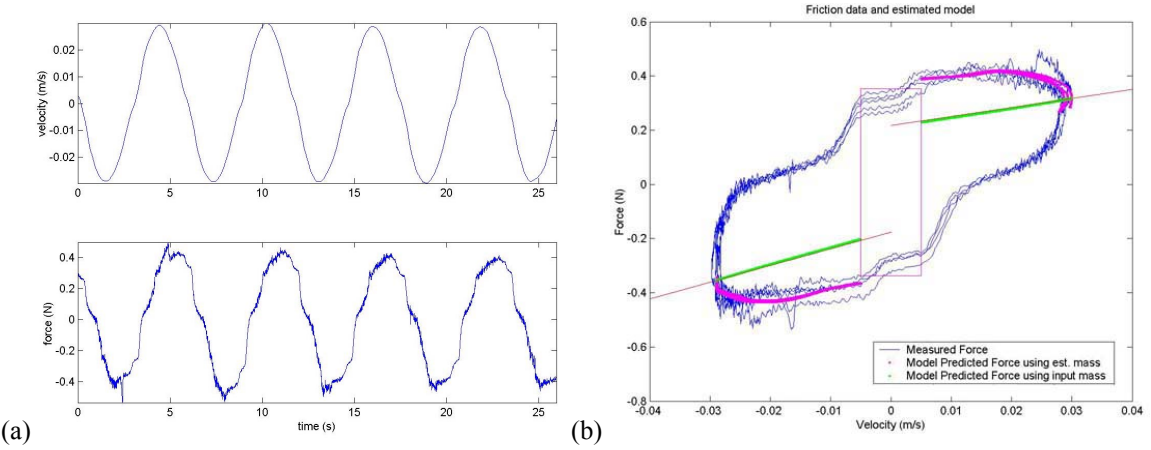


**Figure 34. Friction data for sinusoidal motion of the needle through a 1.95 cm thick liver sample at 0.2 Hz. (a) Velocity and force versus time. (b) Force versus velocity for the orginal data and the modified Karnopp friction model.**

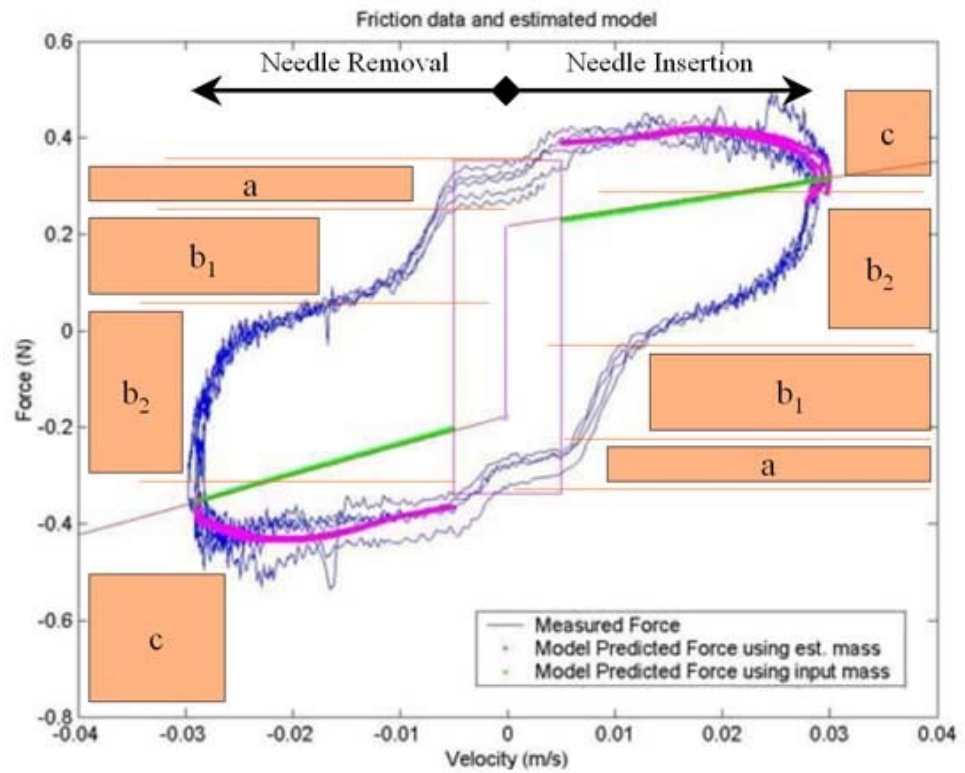


**Figure 35. Force model with actual data. Phases are highlighted.**

The parameters for liver 3 are as follows. The average positive damping value,  $b_p$  per unit length of needle in tissue, was  $556 \text{ Ns/m}^2$ , and the average negative damping value,  $b_n$  per unit length of needle in tissue, was  $294 \text{ Ns/m}^2$ . The values of the damping coefficients varied widely for the different frequencies (we recorded a maximum  $1327 \text{ Ns/m}^2$  of at  $0.2 \text{ Hz}$  and a minimum of  $377 \text{ Ns/m}^2$  at  $0.8 \text{ Hz}$ ), indicating that a more complex model is warranted if differing needle insertion speeds are to be used. The average positive and negative coefficients of dynamic friction ( $C_p$  and  $C_n$ ) were  $3 \text{ N/m}$  and  $10 \text{ N/m}$ , respectively. The average positive and negative coefficients of static friction ( $D_p$  and  $D_n$ ) per unit length of needle in tissue were  $10 \text{ N/m}$  and  $1 \text{ N/m}$ , respectively. Table 4 lists all the values obtained, including overall averages, and averages by insertion frequency, along with standard deviations.

**Table 4. Estimated friction parameters for liver 3. The experiment was performed without the use of imaging.**

Averages by frequency

	freq (Hz)	Cp/ thickness	Bp/ thickness	Cn/ thickness	Bn/ thickness	Dp/ thickness	Dn/ thickness
average	0.2	-7.43797	1154.759	15.24249	811.2653	19.03295	-41.2255
std. Dev.		6.440855	259.0138	9.600668	371.0874	7.04208	7.088462
average	0.5	-0.49856	706.8863	12.42158	591.1764	13.03752	-17.0685
std. Dev.		9.813808	633.3873	3.989373	311.2528	8.478826	34.16312
average	0.8	-5.37755	616.7527	12.87201	213.1772	16.35321	-36.2526
std. Dev.		7.349243	268.8204	10.62808	60.48351	3.716534	21.37294

Total averages

	freq (Hz)	Cp/ thickness	Bp/ thickness	Cn/ thickness	Bn/ thickness	Dp/ thickness	Dn/ thickness
average	0.260355	2.821737	556.4617	9.977761	294.0225	10.39652	0.553738
std. Dev.		7.015221	195.7189	4.108229	223.3635	5.500204	32.80386

The parameters for liver 7 are as follows. The average positive damping value,  $b_p$ , per unit length of needle in tissue, was  $184 \text{ Ns/m}^2$ , and the average negative damping value,  $b_n$ , per unit length of needle in tissue, was  $166 \text{ Ns/m}^2$ . At a slow insertion speed (frequency of 0.2 Hz), a maximum of  $289 \text{ Ns/m}^2$  was recorded, while a minimum of  $79 \text{ Ns/m}^2$  was determined at a faster insertion speed (frequency of 0.5 Hz). This variation indicated that a more complex model is warranted if differing needle insertion speeds are to be used. The average positive and negative coefficients of dynamic friction ( $C_p$  and  $C_n$ ) per unit length of needle in tissue were  $8 \text{ N/m}$  and  $11 \text{ N/m}$ , respectively. The average positive and negative coefficients of static friction ( $D_p$  and  $D_n$ ) per unit length of needle in tissue were  $15 \text{ N/m}$  and  $-18 \text{ N/m}$ , respectively. Table 5 lists all the values obtained, including overall averages, and averages by insertion frequency, along with standard deviations.

**Table 5. Estimated friction parameters for liver 7. The experiment was performed under CT Fluoro imaging.**

Averages by frequency

	m_est	freq (Hz)	Cp/thickness	Bp/thickness	Cn/thickness	Bn/thickness	Dp/thickness	Dn/thickness
average	-2.42504	0.2	10.57252	212.3097	11.95896	293.0829	18.4515	-18.234
std. Dev.	0.628006		4.339624	45.70364	4.404723	30.73343	5.425011	4.301665
average	-0.47486	0.5	9.033673	155.3837	14.18541	114.3228	16.73716	-17.1739
std. Dev.	0.206797		3.59621	66.71168	4.402643	75.95946	2.592235	4.323535
average	-0.78126	0.8	4.931351	184.171	7.187526	90.56273	9.017603	-17.9783
std. Dev.	0.202965		4.632052	18.33471	6.634609	76.00772	2.213596	3.402063

Total averages

	m_est	freq (Hz)	Cp/thickness	Bp/thickness	Cn/thickness	Bn/thickness	Dp/thickness	Dn/thickness
average	-1.22705	0.5	8.17918	183.9548	11.11063	165.9895	14.73542	-17.7954
std. Dev.	0.960353		4.613001	50.42923	5.726098	111.0093	5.455991	3.762079

Although the plates used in these experiments were intended to prevent significant pre-sliding displacement of the liver, some pre-sliding displacement still occurred, resulting in the hysteresis apparent in Figure 34b. The hysteresis in the force versus velocity data may also be due to tissue deflection that is unaccounted for. It can be seen in Figure 34b that most of the friction effects result from Coulomb friction as opposed to viscous damping effects. This is evident from the small slopes ( $b_p$  and  $b_n$ ). The experiments involving CT Fluoro imaging allowed the measurement of relative velocities of the tissue and needle. This makes possible the use of a model that includes pre-sliding displacement, such as a bristle or Dahl friction model [10], which will be considered in future work. It is necessary to note that the algorithm estimated the mass of the needle holder and needle to be negative. This is an indication that there are unmodeled forces present in the data.

An additional factor must be included in the friction model to account for lubrication. In the friction experiments on livers 3 and 7, data was first recorded as the needle passed completely through both sides of the liver to position the needle for sinusoidal velocity. After the needle has passed through both plates, the friction force should remain constant because there is no new tissue to penetrate. However, the measured force has a gentle slope that is visible in Figure 36. The forces rise due to the decreasing lubrication upon continuous insertion into the tissue. This is also observable in the repetitive insertions done at sinusoidal velocities. When the needle moves down into the tissue, it brings liquid that was resting on top of the liver. When the needle comes back up, there is no new lubrication from the other side. This accounts for the slightly

higher forces of the friction vs. velocity plots in the sections where the needle is being removed.

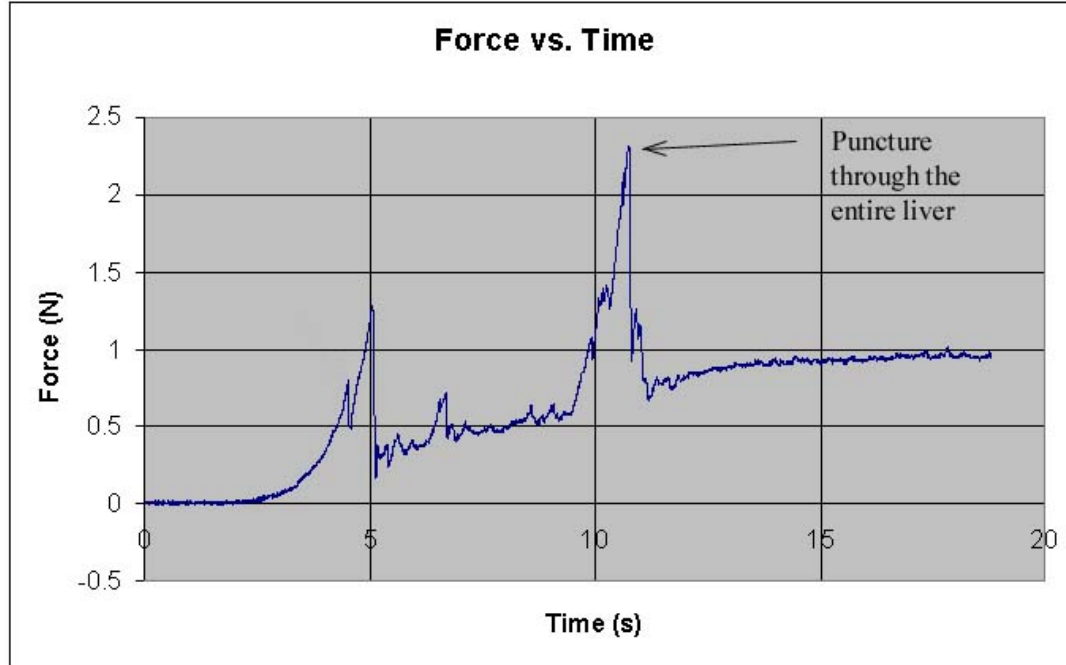


**Figure 36. Forces on the needle tip during insertion. The point at which the entire liver lobe is punctured is denoted. Note the gradual upward slope in forces after this point.**

#### 4.1.3 Cutting

The cutting force is the force that is necessary to slice through the tissue at the tip of the needle. It is postulated that this force for the interior tissue of the liver corresponds to the force required to puncture the liver without its capsule. Ideally, cutting forces will be constant, and therefore unrelated to needle depth. The relation for cutting force is given by

$$f_{cutting} = \begin{cases} 0 & x_{tip} \leq x_{s2}, t < t_p \\ a & x_{tip} > x_{s3}, t \geq t_p \end{cases}, \quad (27)$$

where  $a$  is a constant for a given tissue,  $x_{tip}$  and  $x_{s2}, x_{s3}$  are the position of the needle tip and tissue surface relative to a fixed coordinate system before puncture,  $t$  is time, and  $t_p$  is the time of puncture. Equation 27 assumes that the depth of the needle tip in the tissue monotonically increases with time.

The cutting force is isolated by obtaining the average puncture force of the interior tissue from the internal stiffness/cutting experiment on liver 7. For seven needle insertions at 2.5 mm/s, the average cutting force was 0.0858 N. It is known that the cutting force is due only to cutting in the data sets because there were no collisions with internal vessels near the surface of the tissue. These occurred later in the insertion, as evidenced by sharp increases in the force. These internal collisions add an additional stiffness force that should not be taken into account when measuring the cutting force of the liver tissue. An example of cutting forces is shown in Figure 37.

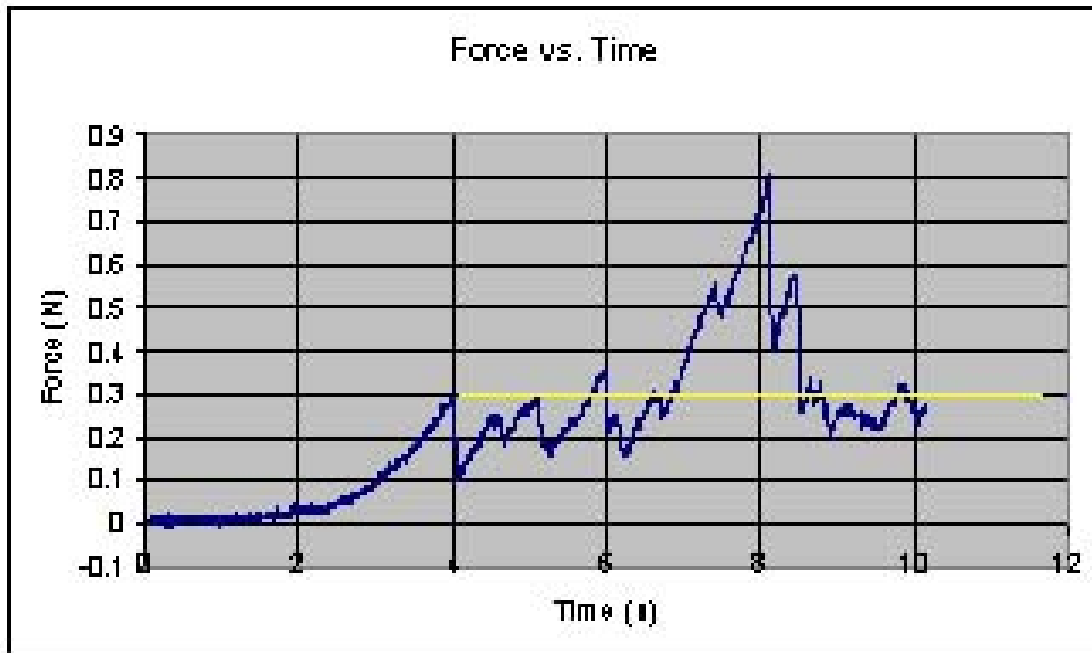


**Figure 37. Forces on the needle during insertion with the average cutting force value marked.**

It is necessary to note that the needle used in the experiment had a blunt tip to obtain stiffness curves for the internal tissue. Therefore, the value for cutting force obtained in this manner does not accurately correspond to the cutting force during a surgical procedure with a sharp tip.

## **4.2 Model Validation**

Use of the model developed in the previous sections necessitates validation by comparison with additional needle insertions. The model is validated by direct comparison of simulated and real data. Based on the average parameter values obtained in the previous section, a complete model of the needle insertion experience has been created. The model, as well as data from real needle insertions, can be compared in Figure 38. The overall shape of the model is similar to the data, although the significant variations in the data from one liver to the next make a perfect match nearly impossible. One problem is that collisions with small interior structures such as blood vessels are not included in the model. These add additional peaks and stiffness forces to the data. Despite these limitations, the model may be still be used for event detection and haptic simulations.

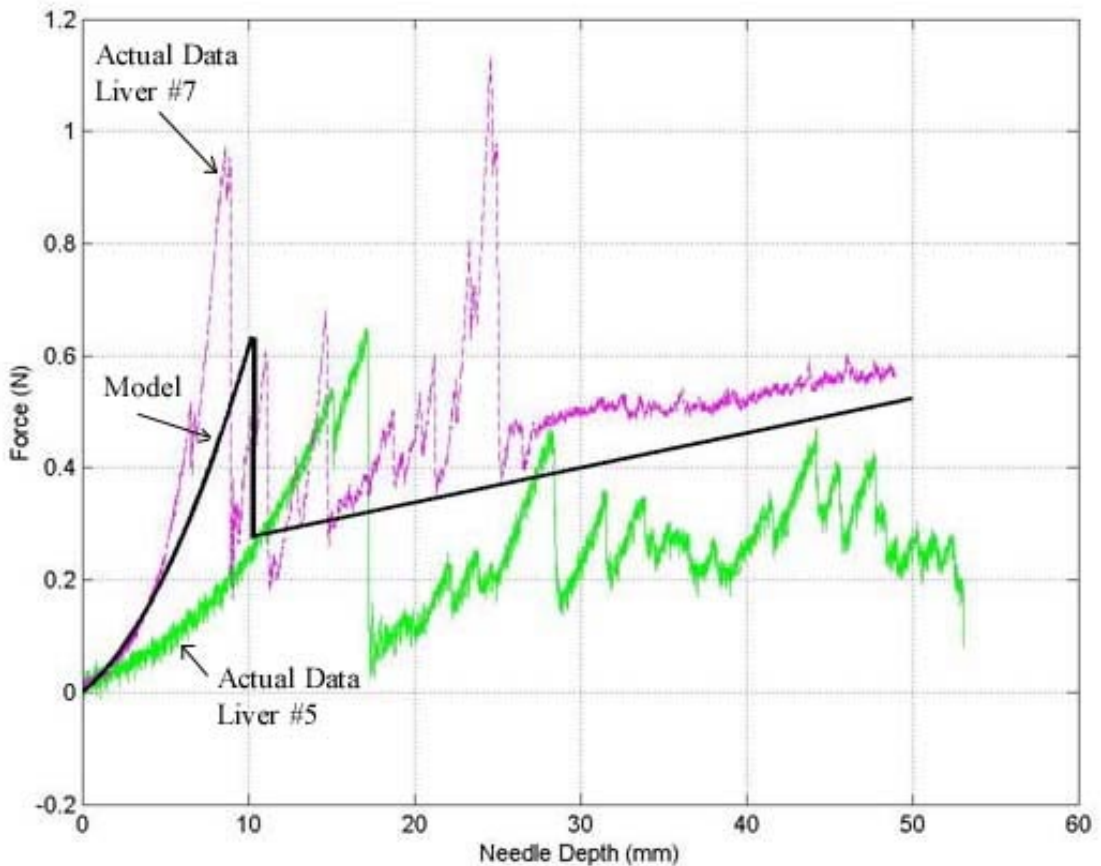


**Figure 38.** The needle insertion model is compared to two insertions on real livers. Although the general shape is similar, the model cannot exactly match the data because of the wide variation in insertion forces and collisions with unmodeled internal structures.

## **5 Prostate Experiment**

A stiffness experiment was performed on the prostate of a canine cadaver. The purpose of this experiment was to begin to quantify the forces during needle insertion into a prostate. Brachytherapy is a percutaneous procedure in which needles are passed through the perineum (the area of skin between the base of the testicles and anus) into the prostate.

*Procedure:*

A fresh (about 2-hour old) beagle cadaver (of approximately 31 kg) was prepared by shaving the perineum and placing the body supine in a wooden platform built for that purpose. The robotic insertion stage was mounted to a passive arm and attached to the platform. A diamond tip needle was inserted at a constant velocity of 4 mm/s through the perineum into the prostate. The abdomen was opened to expose the prostate for visual verification of needle placement. The setup can be seen in Figure 39. 9 data sets were obtained from the canine prostate. Since the canine used in this experiment had been castrated, its prostate was smaller than it would have otherwise been. It is not known whether the forces would be different for a normal-sized prostate.



**Figure 39. Data acquisition on a canine cadaver prostate.**

### **5.1 Data Discussion**

Numerous constant velocity insertions at 4 mm/s within were performed on the canine prostate. A typical force profile from a needle insertion is shown in Figure 40. It is notable that there are many internal punctures. Unfortunately, without the use of an imaging system, it is not possible to determine which punctures correspond only to the prostate. Future experiments should combine data acquisition with imaging to determine at which point the prostate is punctured, as opposed to other neighboring tissue.

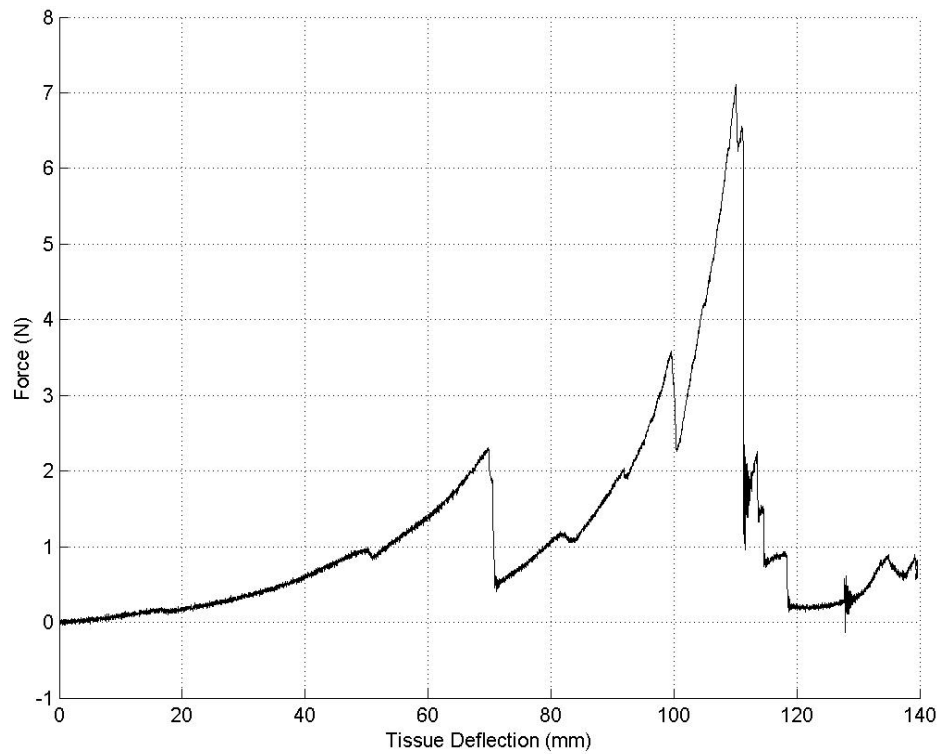


**Figure 40.** A complete plot of needle insertion forces on a canine prostate. There are several internal punctures.

## 6 Conclusion

Automatic compensation for variations in forces and deformation that arise during needle insertion is a worthwhile concept to implement into computer integrated surgical systems. A robotic environment performs well in situations where precision, accuracy and fine control over the instrument motion are vital, such as in percutaneous needle insertions. Autonomous and robot-assisted procedures can compare real-time forces against stored models in order to detect and identify events, thereby responding immediately and appropriately. Before real-time robot reaction to forces for assisted or autonomous needle insertions can be implemented, the insertion forces must first be characterized. Biomechanical modeling allows for tissue boundaries to be detected during percutaneous intervention. The work presented in this thesis has resulted in a methodology for such a characterization.

The models presented here can then be integrated into assistive procedures, autonomous procedures, and haptic virtual environments. Benefits of a system making use of this modeling include improved event detection and reaction time, guidance of velocity and position, and increased accuracy and reliability. Applications include various image-guided percutaneous therapies, such as liver ablation and prostate brachytherapy. Eventually, once these techniques are perfected, it may even be possible to limit the amount of intra-operative imaging in percutaneous procedures, thereby providing the added benefit of minimizing X-ray exposure to operating room staff and patients.

## **6.1 Contributions**

The goal of developing a methodology to model soft tissue interactions with needles has been met. The development of models and their utility in comparisons with real-time force data was demonstrated. Data was acquired using needles of two differing tip types: beveled and diamond. Modeling of forces was completed using bovine livers. Also, a preliminary experiment was performed on a canine prostate. An advantage over other force modeling methods currently reported is that the forces are broken down into several components. This division of forces from acquired data has not been previously undertaken. Three main force components were identified: stiffness, friction, and cutting. Using this approach, accurate identification of events during a needle insertion procedure was shown to be possible. Because of unmodeled internal punctures, modeling does not fit actual data exactly. Clearly, further work is necessary to improve the model.

## **6.2 Future Work**

There is a great deal of work that can be done to expand upon all that was accomplished in this project. Before this methodology is sound enough to be used in computer integrated surgical systems, further research is essential to obtain more complete models. There are numerous ways in which these models can be implemented in robot-assisted procedures. Knowledge of the peak force through tissue may be used to limit velocity and guide the needle before puncture. The needle could be made to stop at a specified location, or stop upon an event such as puncture. In addition, the needle could be automatically withdrawn slightly to account for tissue relaxation after puncture. Once it is known that the needle has entered the desired organ, it may use the real-time force

measurements to detect undesired collision and accordingly stop the motion. It would also be possible to maintain relative zero motion of a needle with respect to the tissue by ensuring that the forces remain at a constant level, accounting for motion of organs due to respiration.

Before this work is deemed acceptable in a clinical setting, it should be validated in many different situations. It would be desirable to perform *in vivo* clinical experiments where data would be gathered during an actual procedure. However, before this is able to occur, the system must be considered safe enough for use with a patient.

The Steady-Hand Robot can additionally be used for the haptic display of stiffness for use in simulations. For clinical trials and use, a different method of gripping the needle would need to be implemented so that the hub of the needle would be accessible, while still permitting a force sensor attached to the needle to read tissue interaction forces. The user would grasp a handle on the end-effector, and the applied forces (conveyed by a separate 6-DOF force sensor) would be used by the robot control system to guide the robot by complying with those forces.

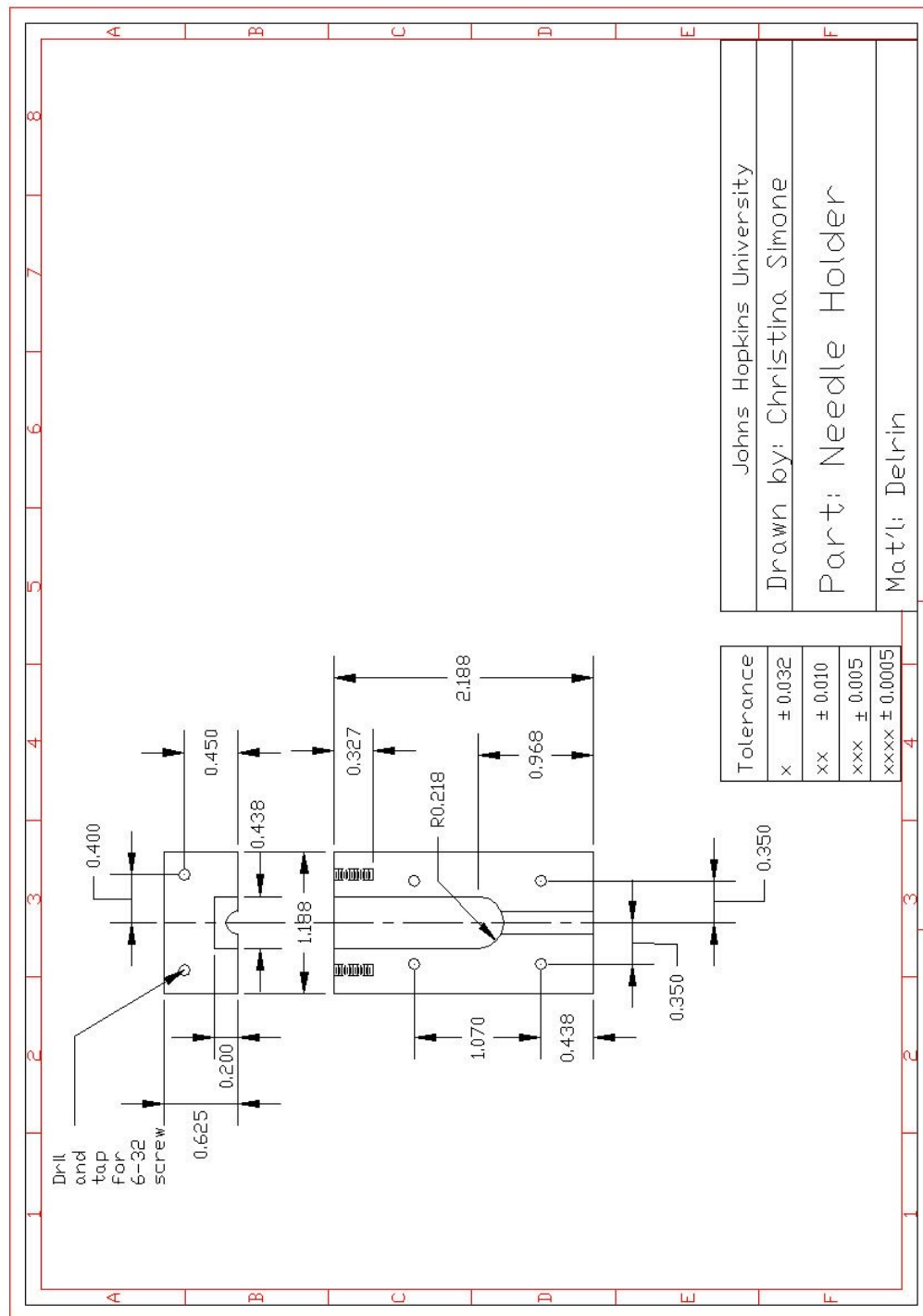
Several areas that can benefit from additional study are outlined below:

- While the primary direction of force is exerted along the axis of the needle, further experiments may want to make use of a 6-axis force-torque load cell to take any extraneous moments into account.
- An accelerometer can be incorporated to obtain vibration measurements for event detection.
- The protocol may be used to model other organs.
- Diseased organs can be modeled for comparison to normal organs.

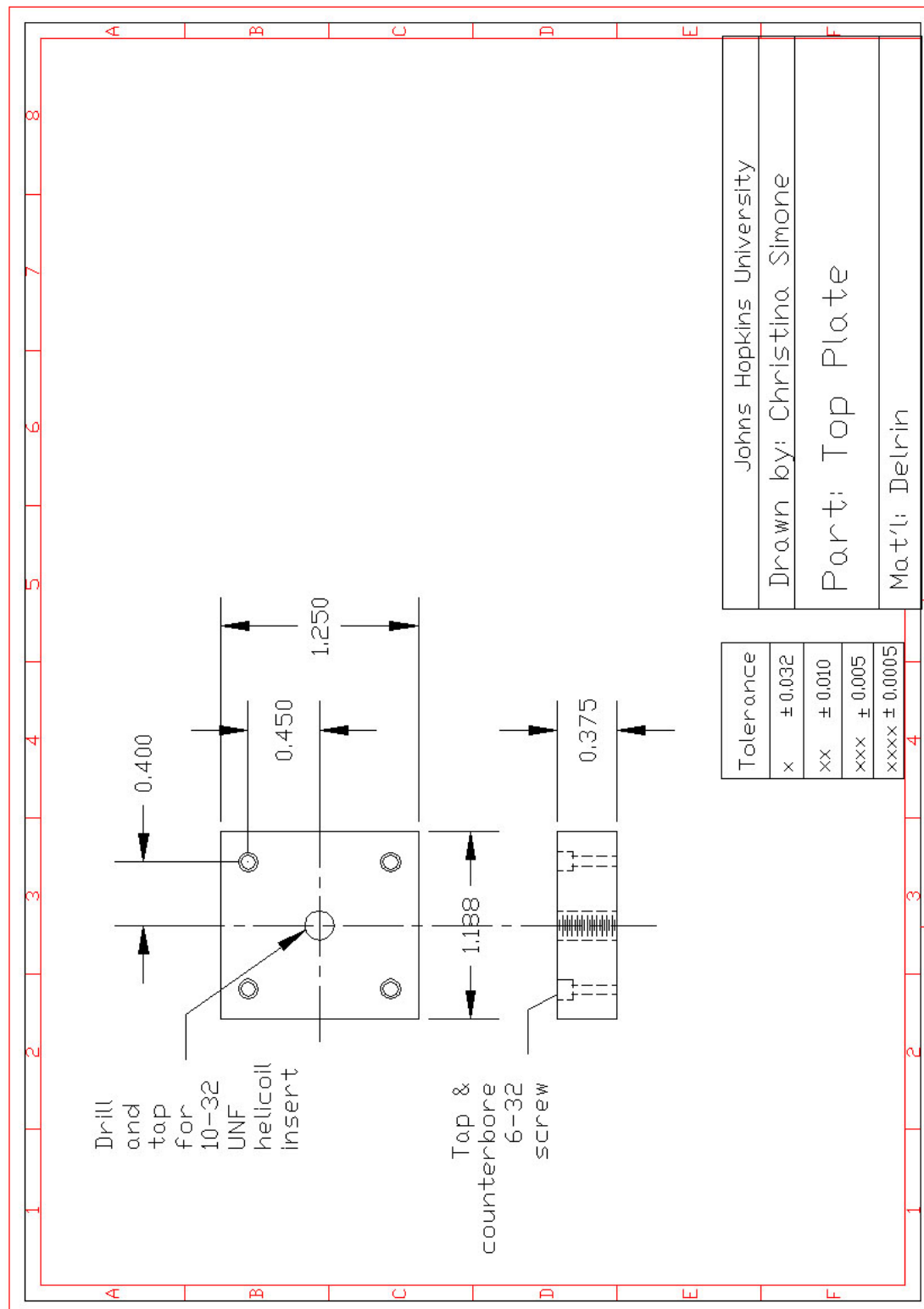
- Future experiments could include needles of differing gages and cutting tips.
- Implement rotation of the needle about its axis during insertion to determine if friction can be reduced.
- More complete biomechanical models including viscoelasticity should be tested for the pre-puncture data.

## Appendix A: Mechanical Drawings

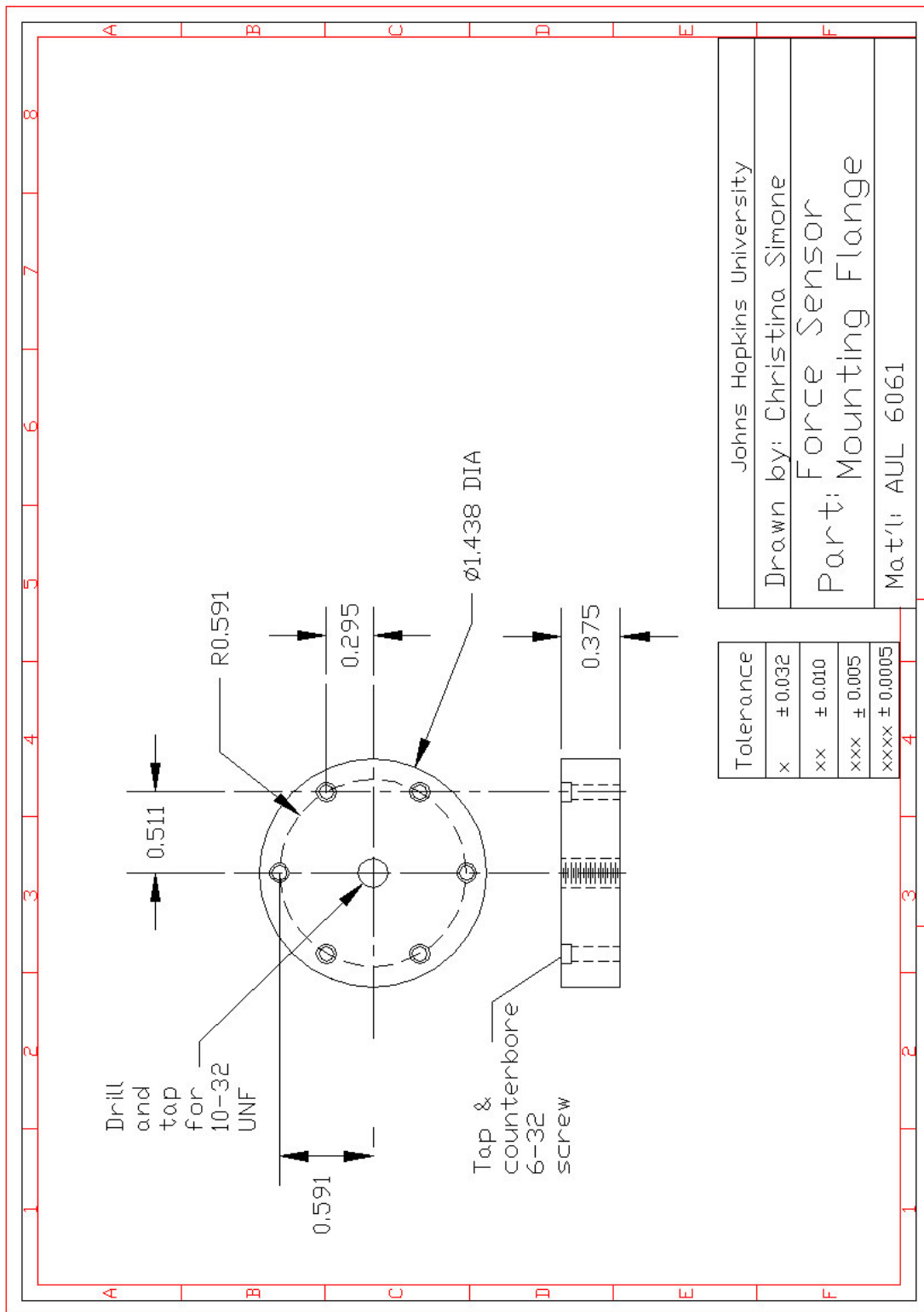
### A.1 Needle Holder



## *A.2 Top Plate*

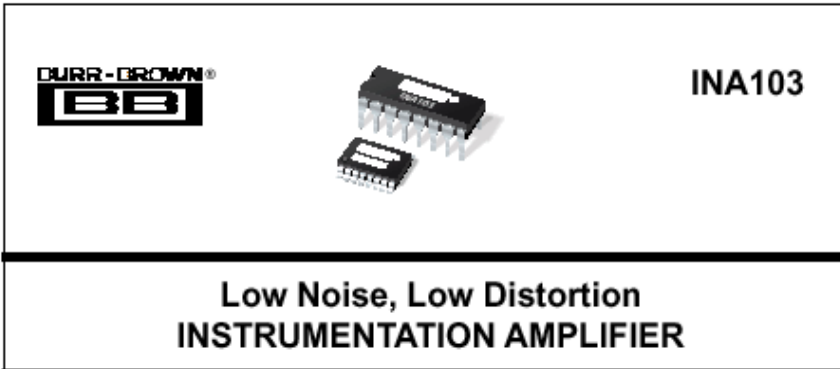


### A.3 Force Sensor Mounting Flange

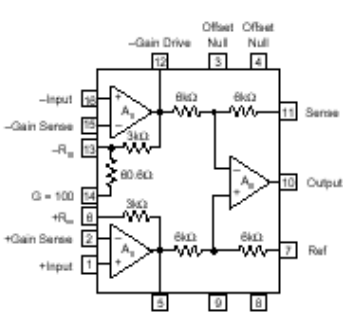


## Appendix B: Data Sheets

### B.1 INA103 Instrumentation Amplifier



The cover of the INA103 datasheet features the Burr-Brown logo (BB) and the part number INA103. Below the title, it highlights "Low Noise, Low Distortion INSTRUMENTATION AMPLIFIER".

<p><b>FEATURES</b></p> <ul style="list-style-type: none"><li>● LOW NOISE: <math>1\text{nV}/\sqrt{\text{Hz}}</math></li><li>● LOW THD+N: 0.0009% at 1kHz, <math>G = 100</math></li><li>● HIGH GBW: 100MHz at <math>G = 1000</math></li><li>● WIDE SUPPLY RANGE: <math>\pm 9\text{V}</math> to <math>\pm 25\text{V}</math></li><li>● HIGH CMRR: &gt;100dB</li><li>● BUILT-IN GAIN SETTING RESISTORS: <math>G = 1, 100</math></li><li>● UPGRADES AD625</li></ul>	<p><b>APPLICATIONS</b></p> <ul style="list-style-type: none"><li>● HIGH QUALITY MICROPHONE PREAMPS (REPLACES TRANSFORMERS)</li><li>● MOVING-COIL PREAMPLIFIERS</li><li>● DIFFERENTIAL RECEIVERS</li><li>● AMPLIFICATION OF SIGNALS FROM: Strain Gages (Weigh Scale Applications) Thermocouples Bridge Transducers</li></ul>
<p><b>DESCRIPTION</b></p> <p>The INA103 is a very low noise, low distortion monolithic instrumentation amplifier. Its current-feedback circuitry achieves very wide bandwidth and excellent dynamic response. It is ideal for low-level audio signals such as balanced low-impedance microphones. The INA103 provides near-theoretical limit noise performance for <math>200\Omega</math> source impedances. Many industrial applications also benefit from its low noise and wide bandwidth.</p> <p>Unique distortion cancellation circuitry reduces distortion to extremely low levels, even in high gain. Its balanced input, low noise and low distortion provide superior performance compared to transformer-coupled microphone amplifiers used in professional audio equipment.</p> <p>The INA103's wide supply voltage (<math>\pm 9</math> to <math>\pm 25\text{V}</math>) and high output current drive allow its use in high-level audio stages as well. A copper lead frame in the plastic DIP assures excellent thermal performance.</p>	
 <p>The internal circuit diagram of the INA103 shows a differential input stage with two operational amplifiers, <math>A_1</math> and <math>A_2</math>. The non-inverting input (+Input) is connected to <math>A_1</math>, and the inverting input (-Input) is connected to <math>A_2</math>. Both inputs have feedback resistors of <math>8k\Omega</math> and <math>80.8k\Omega</math> respectively. The outputs of <math>A_1</math> and <math>A_2</math> are connected to a summing junction with a <math>3k\Omega</math> resistor. The output of this junction is fed into a second stage consisting of two operational amplifiers, <math>A_3</math> and <math>A_4</math>. The non-inverting input of <math>A_3</math> is connected to the output of <math>A_2</math>, and its inverting input is connected to the output of <math>A_1</math>. The output of <math>A_3</math> is connected to the inverting input of <math>A_4</math>, and its non-inverting input is connected to a <math>6k\Omega</math> resistor. The output of <math>A_4</math> is the final output. The circuit also includes offset nulling controls (Offset Null, Null, Null) and a reference rail (Ref). Power supply connections include +Gain Drive, V+, and V-.</p>	

## SPECIFICATIONS

All specifications at  $T_{\text{a}} = +25^{\circ}\text{C}$ ,  $V_{\text{g}} = \pm 15\text{V}$  and  $R_{\text{g}} = 2\text{k}\Omega$ , unless otherwise noted.

PARAMETER	CONDITIONS	INA103KP, KU			UNITS
		MIN	TYP	MAX	
<b>GAIN</b>					
Range of Gain		1			
Gain Equation <sup>(3)</sup>			$G = 1 + 8k\omega R_{\text{g}}$		
Gain Error, DC $G = 1$	$\pm 10\text{V}$ Output		0.005	0.05	%
$G = 100$			0.07	0.25	%
Equation			0.05		%
Gain Temp. Co. $G = 1$	$\pm 10\text{V}$ Output		10		$\text{ppm}/^{\circ}\text{C}$
$G = 100$			25		$\text{ppm}/^{\circ}\text{C}$
Equation			25		$\text{ppm}/^{\circ}\text{C}$
Nonlinearity, DC $G = 1$	$\pm 10\text{V}$ Output		0.0003	0.01	% of FS <sup>(4)</sup>
$G = 100$			0.0008	0.01	% of FS
<b>OUTPUT</b>					
Voltage, $R_{\text{o}} = 800\Omega$	$T_{\text{a}} = T_{\text{min}} \text{ to } T_{\text{max}}$	$\pm 11.5$	$\pm 12$		V
$R_{\text{o}} = 800\Omega$	$V_{\text{g}} = \pm 25, T_{\text{a}} = 25^{\circ}\text{C}$	$\pm 20$	$\pm 21$		V
Current	$T_{\text{a}} = T_{\text{min}} \text{ to } T_{\text{max}}$	$\pm 40$			mA
Short Circuit Current			$\pm 70$		mA
Capacitive Load Stability			10		nF
<b>INPUT OFFSET VOLTAGE</b>					
Initial Offset RTI <sup>(5)</sup> (KU Grade)			$(30 + 1200/G)$		$\mu\text{V}$
vs Temp $G = 1$ to 1000	$T_{\text{a}} = T_{\text{min}} \text{ to } T_{\text{max}}$		$1 + 20/G$		$\mu\text{V}$
$G = 1000$	$T_{\text{a}} = T_{\text{min}} \text{ to } T_{\text{max}}$		$0.2 + 8/G$		$\mu\text{V}/^{\circ}\text{C}$
vs Supply	$\pm 9\text{V} \text{ to } \pm 25\text{V}$			$4 + 80/G$	$\mu\text{V}/\text{V}$
<b>INPUT BIAS CURRENT</b>					
Initial Bias Current	$T_{\text{a}} = T_{\text{min}} \text{ to } T_{\text{max}}$		2.5	12	$\mu\text{A}$
vs Temp			15		$\text{nA}/^{\circ}\text{C}$
Initial Offset Current	$T_{\text{a}} = T_{\text{min}} \text{ to } T_{\text{max}}$		0.04	1	$\mu\text{A}$
vs Temp			0.5		$\text{nA}/^{\circ}\text{C}$
<b>INPUT IMPEDANCE</b>					
Differential Mode			$80    2$		$\text{M}\Omega    \text{pF}$
Common-Mode			$80    5$		$\text{M}\Omega    \text{pF}$
<b>INPUT VOLTAGE RANGE</b>					
Common-Mode Range <sup>(6)</sup>		$\pm 11$	$\pm 12$		V
CMR					
$G = 1$	DC to 80Hz	72	88		dB
$G = 100$	DC to 80Hz	100	125		dB
<b>INPUT NOISE</b>					
Voltage <sup>(7)</sup>	$R_{\text{g}} = 0\Omega$				
10Hz			2		$\text{nV}/\sqrt{\text{Hz}}$
100Hz			1.2		$\text{nV}/\sqrt{\text{Hz}}$
1kHz			1		$\text{nV}/\sqrt{\text{Hz}}$
Current, 1kHz			2		$\text{pA}/\sqrt{\text{Hz}}$
<b>OUTPUT NOISE</b>					
Voltage	1kHz		86		$\text{nV}/\sqrt{\text{Hz}}$
A Weighted, 20Hz-20kHz	20Hz-20kHz		-100		dBu
<b>DYNAMIC RESPONSE</b>					
-3dB Bandwidth: $G = 1$	Small Signal		8		MHz
$G = 100$	Small Signal		800		kHz
Full Power Bandwidth	$G = 1$				
$V_{\text{in}} = \pm 10\text{V}, R_{\text{g}} = 800\Omega$			240		kHz
Slew Rate	$G = 1$ to 500		15		V/ $\mu\text{s}$
THD + Noise	$G = 100, f = 1\text{kHz}$		0.0009		%
Settling Time 0.1%	$V_{\text{in}} = 20\text{V}$ Step		1.7		$\mu\text{s}$
$G = 1$			1.5		$\mu\text{s}$
$G = 100$					
Settling Time 0.01%	$V_{\text{in}} = 20\text{V}$ Step		2		$\mu\text{s}$
$G = 1$			3.5		$\mu\text{s}$
$G = 100$			1		$\mu\text{s}$
Overload Recovery <sup>(8)</sup>	50% Overdrive				

NOTES: (1) Gains other than 1 and 100 can be set by adding an external resistor,  $R_{\text{g}}$ , between pins 2 and 15. Gain accuracy is a function of  $R_{\text{g}}$ . (2) FS = Full Scale. (3) Adjustable to zero. (4)  $V_{\text{g}} = 0\text{V}$ ; see Typical Curves for  $V_{\text{in}}$  vs  $V_{\text{g}}$ . (5)  $V_{\text{in}} = (V_{\text{in}} + (V_{\text{g}} - V_{\text{in}})/\text{Gain})^2 + 4kT_{\text{in}}$ . See Typical Curves. (6) Time required for output to return from saturation to linear operation following the removal of an input overdrive voltage.

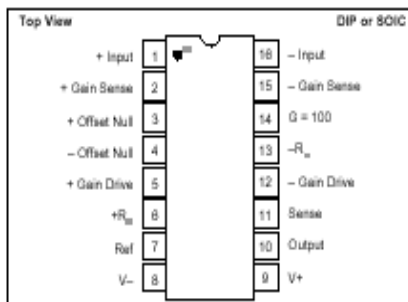


## SPECIFICATIONS (CONT)

All specifications at  $T_a = +25^\circ\text{C}$ ,  $V_a = \pm 15\text{V}$  and  $R_o = 2\text{k}\Omega$ , unless otherwise noted.

PARAMETER	CONDITIONS	INA103KP, KU			UNITS
		MIN	TYP	MAX	
POWER SUPPLY					
Rated Voltage		$\pm 9$	$\pm 15$	$\pm 25$	V
Voltage Range			9	12.5	V
Quiescent Current					mA
TEMPERATURE RANGE					
Specification		0		+70	$^\circ\text{C}$
Operation		-40		+85	$^\circ\text{C}$
Storage		-40		+100	$^\circ\text{C}$
Thermal Resistance, $\theta_{\text{JA}}$			100		$^\circ\text{C}/\text{W}$

### PIN CONFIGURATION



NOTE: (1) Pin 1 Marking—SOI-16 Package

### PACKAGE/ORDERING INFORMATION

PRODUCT	PACKAGE	PACKAGE DRAWING NUMBER <sup>(1)</sup>	TEMPERATURE RANGE
INA103KP	Plastic DIP	180	0°C to +70°C
INA103KU	SOI-16	211	0°C to +70°C

NOTE: (1) For detailed drawing and dimension table, please see end of data sheet or Appendix C of Burr-Brown IC Data Book.

### ELECTROSTATIC DISCHARGE SENSITIVITY

Any integrated circuit can be damaged by ESD. Burr-Brown recommends that all integrated circuits be handled with appropriate precautions. Failure to observe proper handling and installation procedures can cause damage.

ESD damage can range from subtle performance degradation to complete device failure. Precision integrated circuits may be more susceptible to damage because very small parametric changes could cause the device not to meet published specifications.

### ABSOLUTE MAXIMUM RATINGS<sup>(1)</sup>

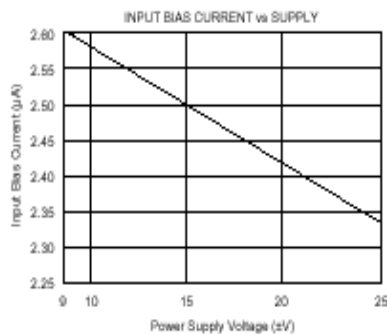
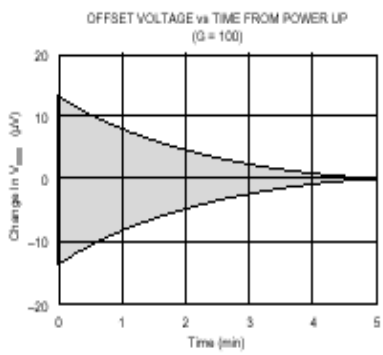
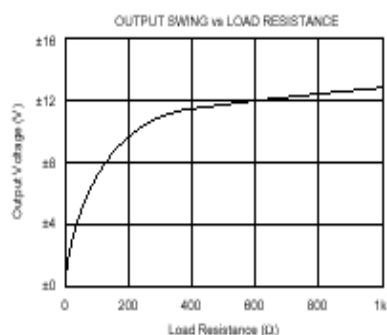
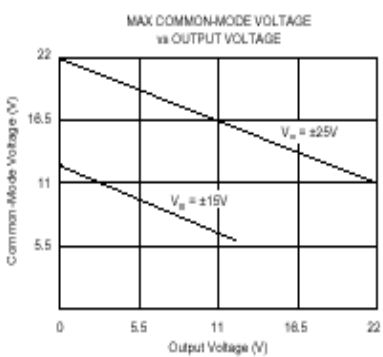
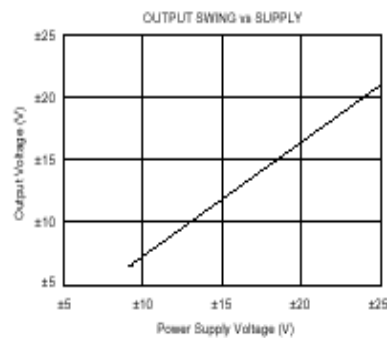
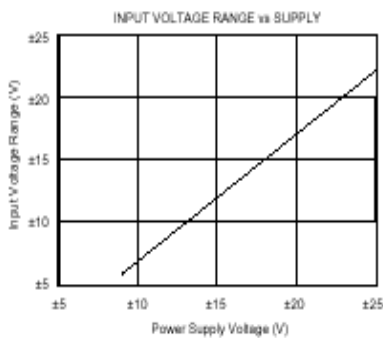
Power Supply Voltage	$\pm 25\text{V}$
Input Voltage Range, Continuous	$\pm V_a$
Operating Temperature Range	-40°C to +85°C
Storage Temperature Range	-40°C to +85°C
Junction Temperature	
P, U Package	+125°C
Lead Temperature (soldering, 10s)	+300°C
Output Short Circuit to Common	Continuous

NOTE: (1) Stresses above these ratings may cause permanent damage.

The information provided herein is believed to be reliable; however, BURR-BROWN assumes no responsibility for inaccuracies or omissions. BURR-BROWN assumes no responsibility for the use of this information, and all use of such information shall be entirely at the user's own risk. Prices and specifications are subject to change without notice. No patent rights or licenses to any of the circuits described herein are implied or granted to any third party. BURR-BROWN does not authorize or warrant any BURR-BROWN product for use in life support devices and/or systems.

## TYPICAL PERFORMANCE CURVES

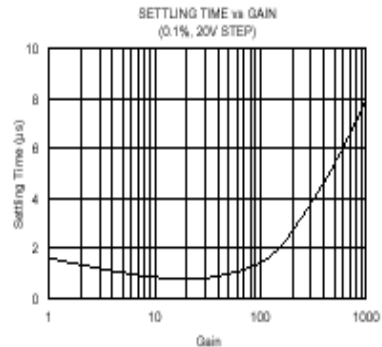
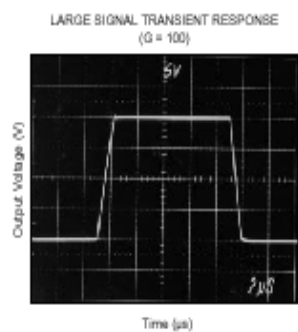
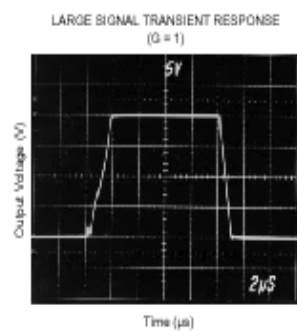
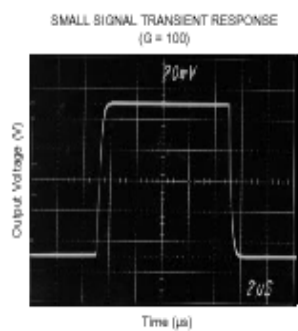
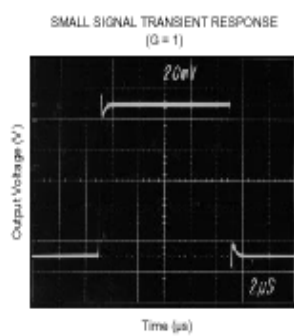
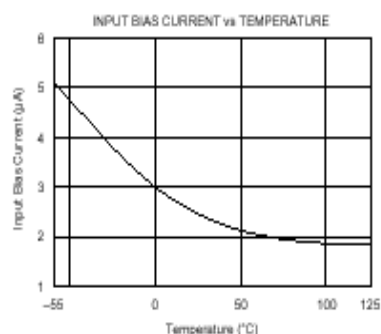
At  $T_a = +25^\circ\text{C}$ ,  $V_a = \pm 15\text{V}$ , unless otherwise noted.



**INA103**

## TYPICAL PERFORMANCE CURVES (CONT)

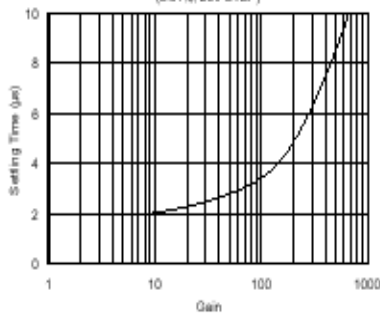
At  $T_c = +25^\circ\text{C}$ ,  $V_c = \pm 15\text{V}$ , unless otherwise noted.



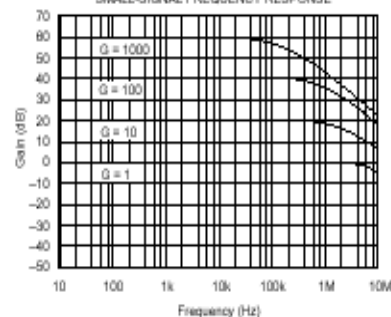
## TYPICAL PERFORMANCE CURVES (CONT)

At  $T_a = +25^\circ\text{C}$ ,  $V_u = \pm 15\text{V}$ , unless otherwise noted.

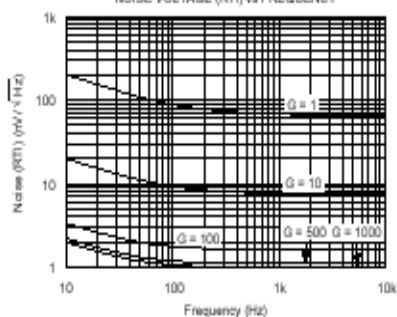
SETTLING TIME vs GAIN  
(0.01%, 20V STEP)



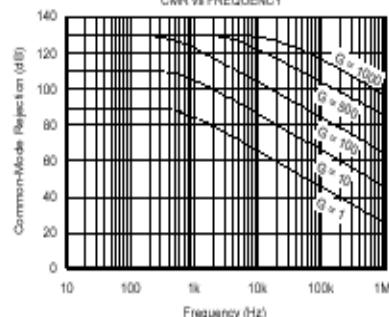
SMALL-SIGNAL FREQUENCY RESPONSE



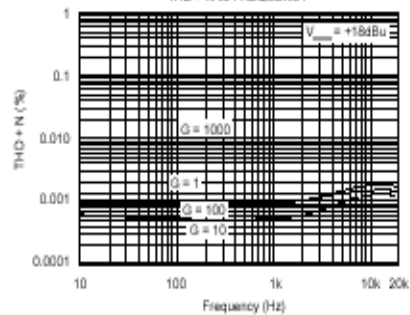
NOISE VOLTAGE (RTI) vs FREQUENCY



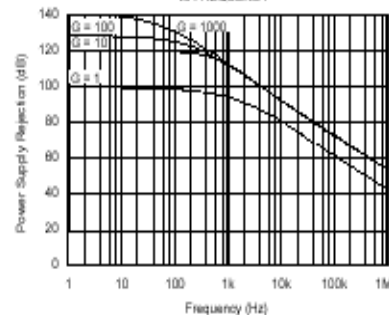
CNR vs FREQUENCY



THD + N vs FREQUENCY



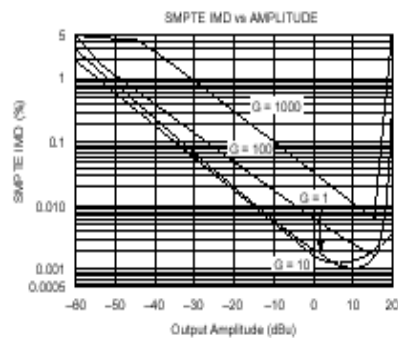
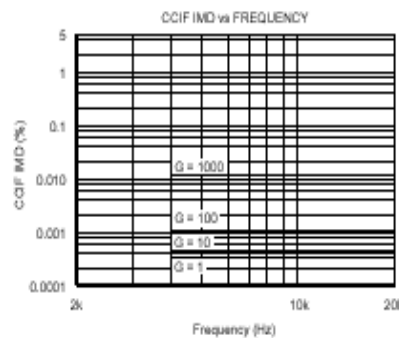
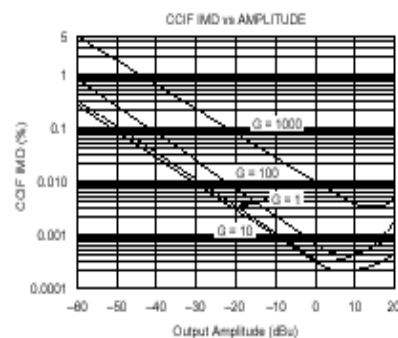
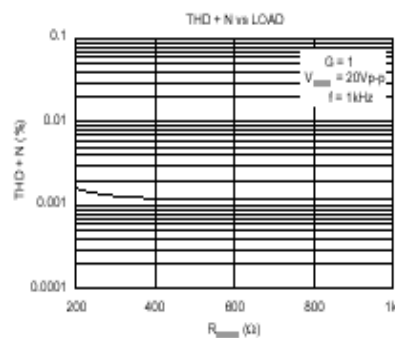
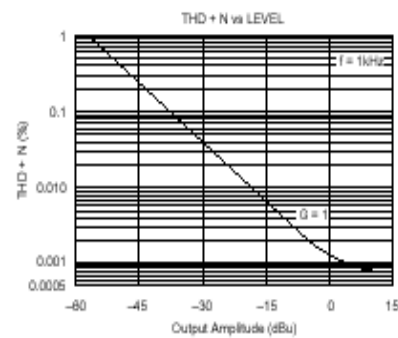
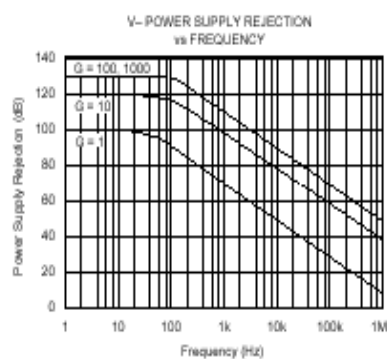
V+ POWER SUPPLY REJECTION  
vs FREQUENCY



**BB** INA103

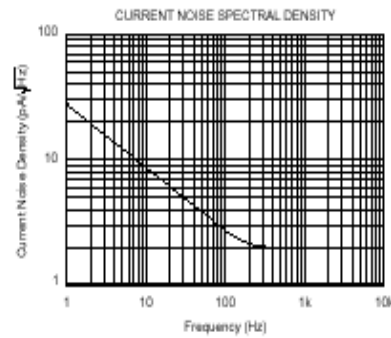
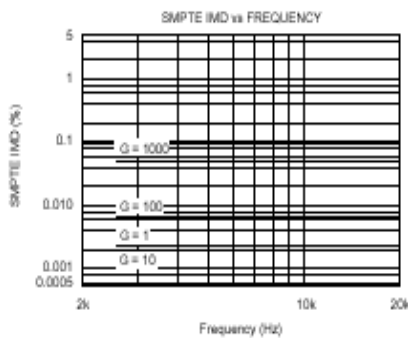
## TYPICAL PERFORMANCE CURVES (CONT)

At  $T_a = +25^\circ\text{C}$ ,  $V_a = \pm 15\text{V}$ , unless otherwise noted.



## TYPICAL PERFORMANCE CURVES (CONT)

At  $T_a = +25^\circ\text{C}$ ,  $V_a = \pm 15\text{V}$  unless, otherwise noted.



## APPLICATIONS INFORMATION

Figure 1 shows the basic connections required for operation. Power supplies should be bypassed with  $1\mu\text{F}$  tantalum capacitors near the device pins. The output Sense (pin 11) and output Reference (pin 7) should be low impedance connections. Resistance of a few ohms in series with these connections will degrade the common-mode rejection of the amplifier. To avoid oscillations, make short, direct connection to the gain set resistor and gain sense connections. Avoid running output signals near these sensitive input nodes.

### INPUT CONSIDERATIONS

Certain source impedances can cause the INA103 to oscillate. This depends on circuit layout and source or cable characteristics connected to the input. An input network consisting of a small inductor and resistor (Figure 2) can greatly reduce the tendency to oscillate. This is especially

useful if various input sources are connected to the INA103. Although not shown in other figures, this network can be used, if needed, with all applications shown.

### GAIN SELECTION

Gains of 1 or 100V/V can be set without external resistors. For  $G = 1\text{V/V}$  (unity gain) leave pin 14 open (no connection)—see Figure 4. For  $G = 100\text{V/V}$ , connect pin 14 to pin 6—see Figure 5.

Gain can also be accurately set with a single external resistor as shown in Figure 1. The two internal feedback resistors are laser-trimmed to  $3\text{k}\Omega$  within approximately  $\pm 0.1\%$ . The temperature coefficient of these resistors is approximately  $50\text{ppm}/^\circ\text{C}$ . Gain using an external  $R_m$  resistor is—

$$G = 1 + \frac{6\text{k}\Omega}{R_m}$$



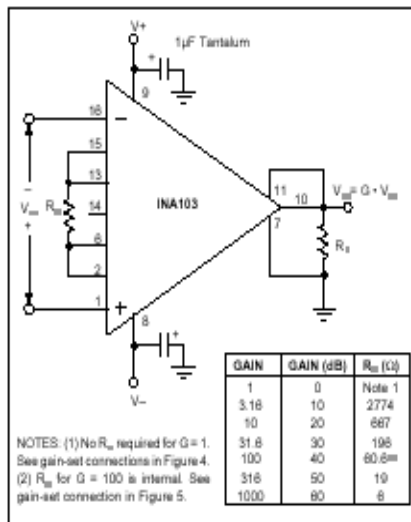


FIGURE 1. Basic Circuit Configuration.

Accuracy and TCR of the external  $R_f$  will also contribute to gain error and temperature drift. These effects can be directly inferred from the gain equation.

Connections available on  $A_g$  and  $A_o$  allow external resistors to be substituted for the internal  $3\text{k}\Omega$  feedback resistors. A precision resistor network can be used for very accurate and stable gains. To preserve the low noise of the INA103, the value of external feedback resistors should be kept low. Increasing the feedback resistors to  $20\text{k}\Omega$  would increase noise of the INA103 to approximately  $1.5\text{nV}/\sqrt{\text{Hz}}$ . Due to the current-feedback input circuitry, bandwidth would also be reduced.

### NOISE PERFORMANCE

The INA103 provides very low noise with low source impedance. Its  $1\text{nV}/\sqrt{\text{Hz}}$  voltage noise delivers near theoretical noise performance with a source impedance of  $200\Omega$ . Relatively high input stage current is used to achieve this low noise. This results in relatively high input bias current and input current noise. As a result, the INA103 may not provide best noise performance with source impedances greater than  $10\text{k}\Omega$ . For source impedance greater than  $10\text{k}\Omega$ , consider the INA114 (excellent for precise DC applications), or the INA111 FET-input IA for high speed applications.

### OFFSET ADJUSTMENT

Offset voltage of the INA103 has two components: input stage offset voltage is produced by  $A_g$  and  $A_o$ ; and, output stage offset is produced by  $A_o$ . Both input and output stage offset are laser trimmed and may not need adjustment in many applications.

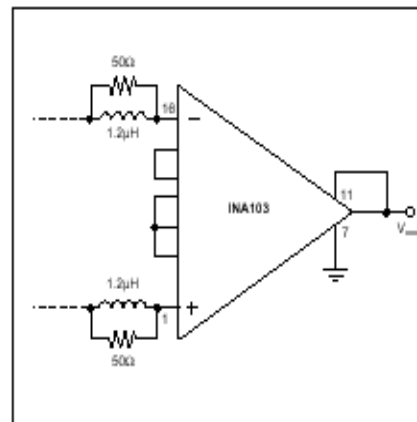


FIGURE 2. Input Stabilization Network.

Offset voltage can be trimmed with the optional circuit shown in Figure 3. This offset trim circuit primarily adjusts the output stage offset, but also has a small effect on input stage offset. For a 1mV adjustment of the output voltage, the input stage offset is adjusted approximately  $1\mu\text{V}$ . Use this adjustment to null the INA103's offset voltage with zero differential input voltage. Do not use this adjustment to null offset produced by a sensor, or offset produced by subsequent stages, since this will increase temperature drift.

To offset the output voltage without affecting drift, use the circuit shown in Figure 4. The voltage applied to pin 7 is summed at the output. The op amp connected as a buffer provides a low impedance at pin 7 to assure good common-mode rejection.

Figure 5 shows a method to trim offset voltage in AC-coupled applications. A nearly constant and equal input bias current of approximately  $2.5\mu\text{A}$  flows into both input terminals. A variable input trim voltage is created by adjusting the balance of the two input bias return resistances through which the input bias currents must flow.

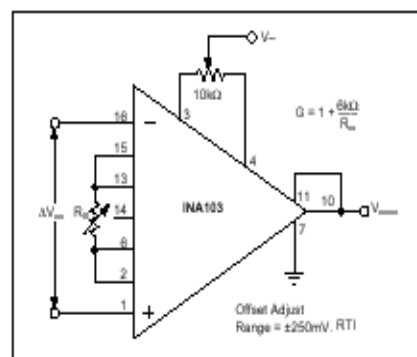


FIGURE 3. Offset Adjustment Circuit.

Figure 6 shows an active control loop that adjusts the output offset voltage to zero.  $A_{v_o}$ , R, and C form an integrator that produces an offsetting voltage applied to one input of the INA103. This produces a  $-6\text{dB/octave}$  low frequency roll-off like the capacitor input coupling in Figure 5.

#### COMMON-MODE INPUT RANGE

For proper operation, the combined differential input signal and common-mode input voltage must not cause the input amplifiers to exceed their output swing limits. The linear input range is shown in the typical performance curve "Maximum Common-Mode Voltage vs Output Voltage." For a given total gain, the input common-mode range can be increased by reducing the input stage gain and increasing the output stage gain with the circuit shown in Figure 7.

#### OUTPUT SENSE

An output sense terminal allows greater gain accuracy in driving the load. By connecting the sense connection at the load,  $1\text{R}$  voltage loss to the load is included inside the feedback loop. Current drive can be increased by connecting a current booster inside the feedback loop as shown in Figure 11.

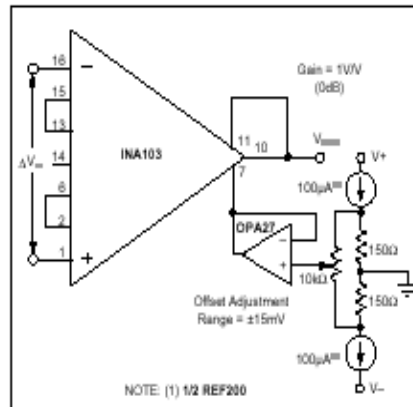


FIGURE 4. Output Offsetting.

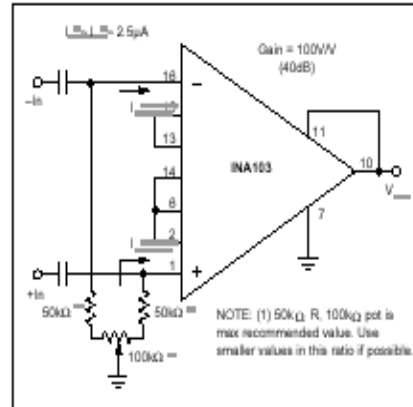


FIGURE 5. Input Offset Adjustment for AC-Coupled Inputs.

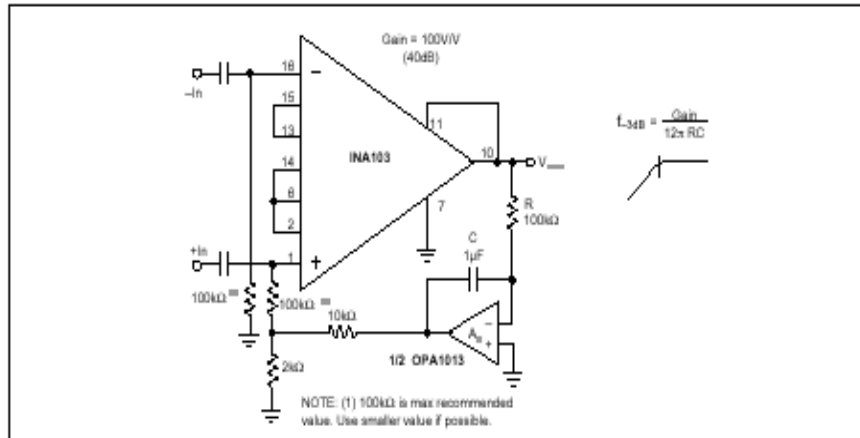


FIGURE 6. Automatic DC Restoration.



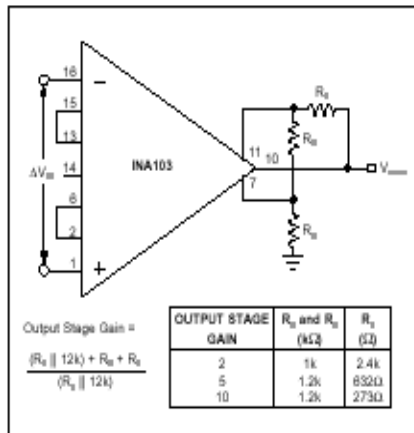


FIGURE 7. Gain Adjustment of Output Stage.

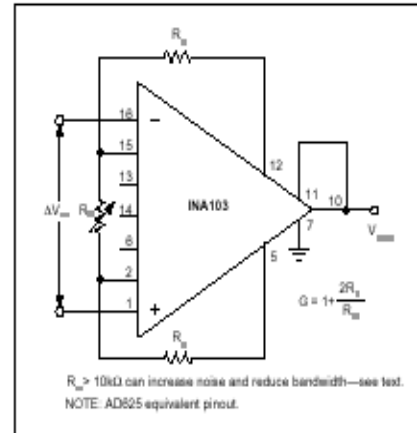
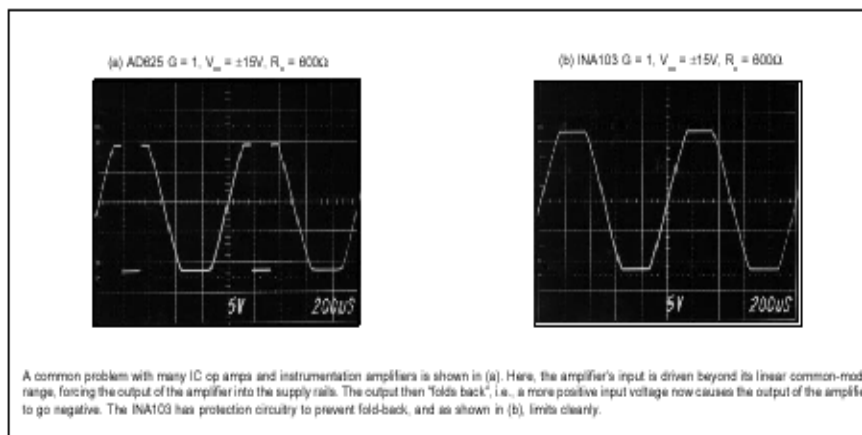


FIGURE 8. Use of External Resistors for Gain Set.



A common problem with many IC op amps and instrumentation amplifiers is shown in (a). Here, the amplifier's input is driven beyond its linear common-mode range, forcing the output of the amplifier into the supply rails. The output then "folds back", i.e., a more positive input voltage now causes the output of the amplifier to go negative. The INA103 has protection circuitry to prevent fold-back, and as shown in (b), limits cleanly.

FIGURE 9. INA103 Overload Condition Performance.

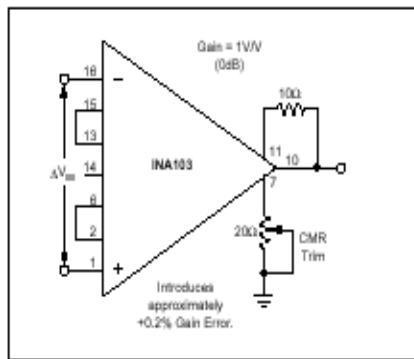


FIGURE 10. Optional Circuit for Externally Trimming CMR.

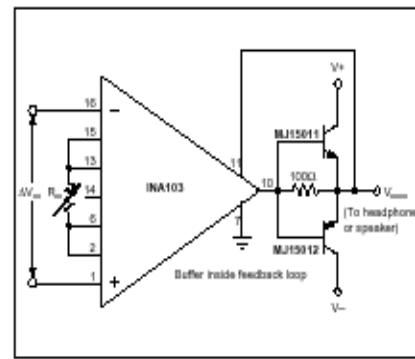


FIGURE 11. Increasing Output Circuit Drive.

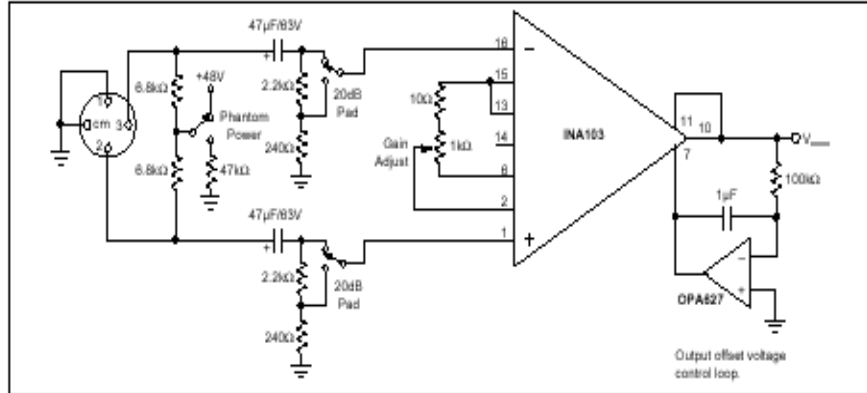


FIGURE 12. Microphone Preamplifier with Provision for Phantom Power Microphones.

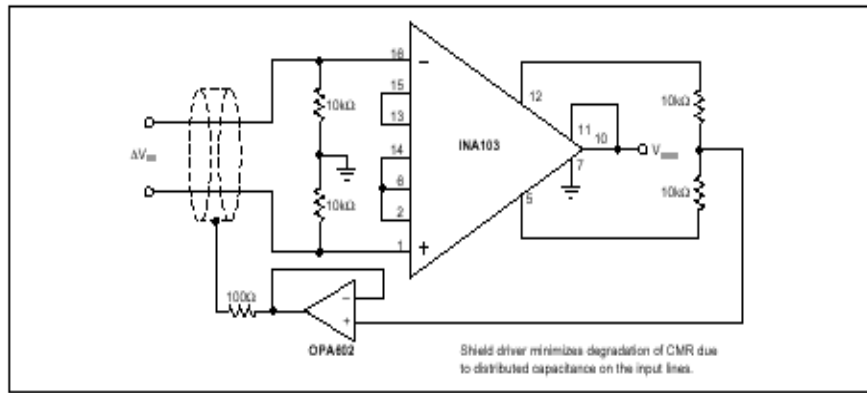


FIGURE 13. Instrumentation Amplifier with Shield Driver.

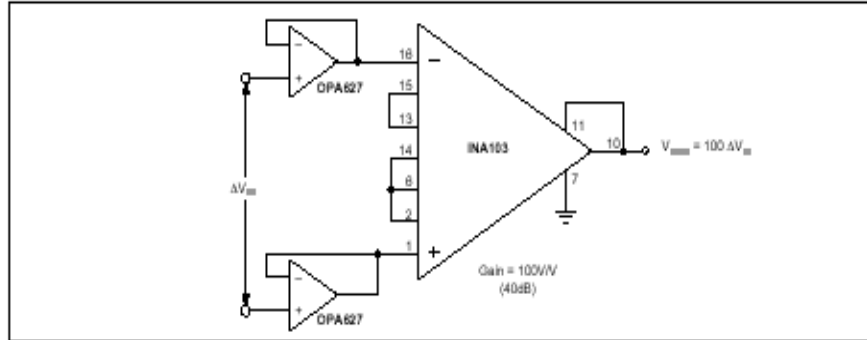


FIGURE 14. Gain-of-100 INA103 with FET Buffers.

**INA103**

#### **IMPORTANT NOTICE**

Texas Instruments and its subsidiaries (TI) reserve the right to make changes to their products or to discontinue any product or service without notice, and advise customers to obtain the latest version of relevant information to verify, before placing orders, that information being relied on is current and complete. All products are sold subject to the terms and conditions of sale supplied at the time of order acknowledgment, including those pertaining to warranty, patent infringement, and limitation of liability.

TI warrants performance of its semiconductor products to the specifications applicable at the time of sale in accordance with TI's standard warranty. Testing and other quality control techniques are utilized to the extent TI deems necessary to support this warranty. Specific testing of all parameters of each device is not necessarily performed, except those mandated by government requirements.

Customers are responsible for their applications using TI components.

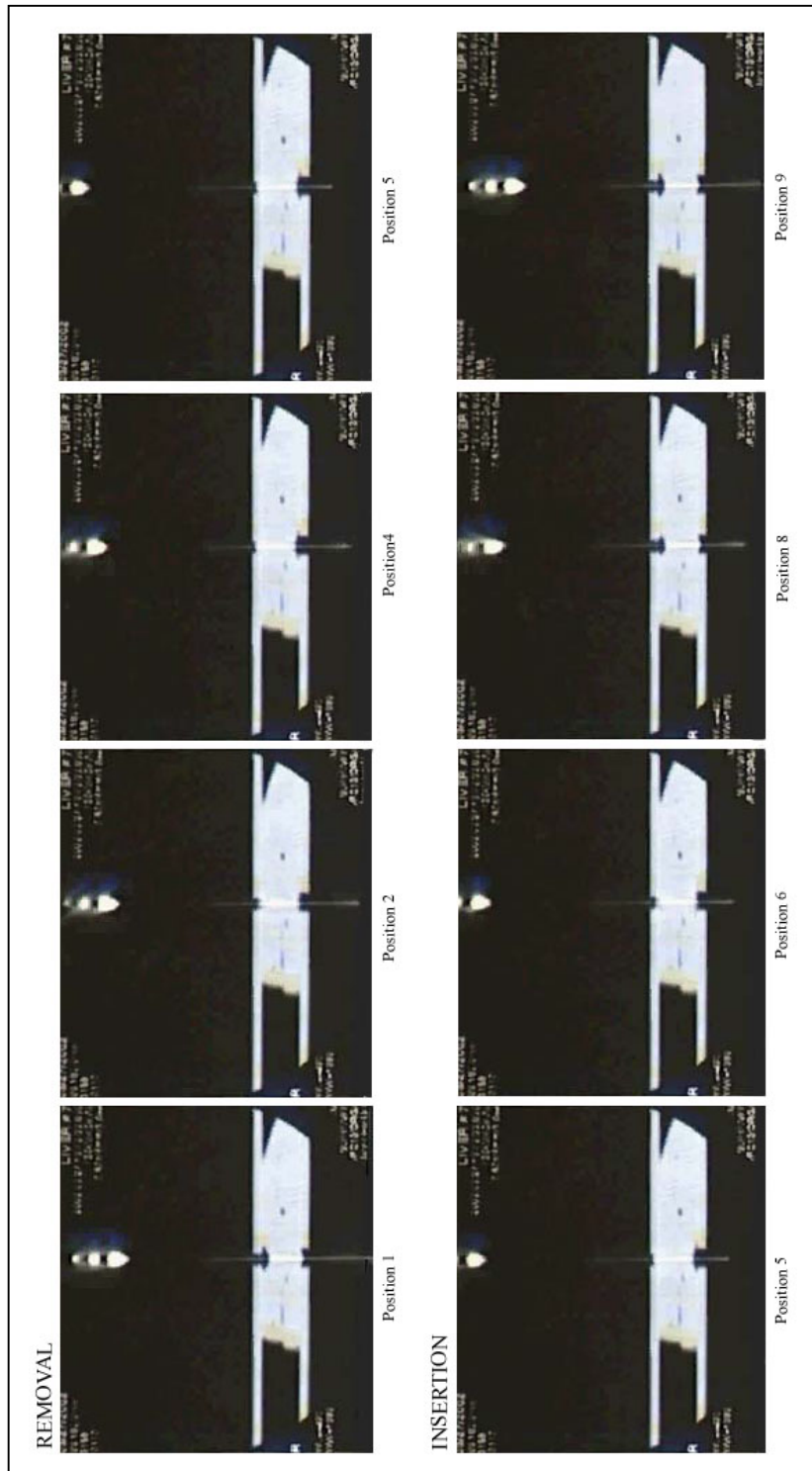
In order to minimize risks associated with the customer's applications, adequate design and operating safeguards must be provided by the customer to minimize inherent or procedural hazards.

TI assumes no liability for applications assistance or customer product design. TI does not warrant or represent that any license, either express or implied, is granted under any patent right, copyright, mask work right, or other intellectual property right of TI covering or relating to any combination, machine, or process in which such semiconductor products or services might be or are used. TI's publication of information regarding any third party's products or services does not constitute TI's approval, warranty or endorsement thereof.

Copyright © 2000, Texas Instruments Incorporated

## Appendix C: CT Fluoro Images

The images shown below are repeated from Figure 32 in Chapter 4.1.2 for clarity.



## Bibliography

- [1] Brett PN, Harrison AJ and Thomas TA. "Schemes for the Identification of Tissue Types and Boundaries at the Tool Point for Surgical Needles," *IEEE Trans. Information Technology in Biomedicine*, Vol. 4, No. 1, 2000, pp. 30-36.
- [2] Brett PN et al. "Simulation of resistance forces acting on surgical needles," *Proceedings of the Institution of Mechanical Engineers, Part H*, Vol. 211 (H4), 1997, pp. 335-347.
- [3] Brouwer I et al. "Measuring In Vivo Animal Soft Tissue Properties for Haptic Modeling in Surgical Simulation," *Medicine Meets Virtual Reality 2001*, pp. 69-74.
- [4] d'Aulignac D, Balaniuk R and Laugier C. "A Haptic Interface for a Virtual Exam of the Human Thigh," *Proceedings of the 2000 IEEE International Conference on Robotics & Automation*, pp. 2452-2456.
- [5] Karnopp D. "Computer Simulation of Stick-Slip Friction in Mechanical Dynamic Systems." *Journal of Dynamic Systems, Measurement and Control, Transactions ASME*. 1985.
- [6] Fung YC. Biomechanics: Mechanical Properties of Living Tissues, 2nd ed., New York: Springer-Verlag, 1993, pp. 277.
- [7] Gobbetti E et al. "Catheter Insertion Simulation with Co-registered Direct Volume Rendering and Haptic Feedback," *Medicine Meets Virtual Reality 2000*, pp. 96-98.

- [8] Gorman P et al. “A Prototype Haptic Lumbar Puncture Simulator,” *Proceedings of Medicine Meets Virtual Reality 2000*, pp. 106-109.
- [9] Hayashi K, Abé H and Sato M. Data Book on Mechanical Properties of Living Cells, Tissues, and Organs, New York: Springer, 1996.
- [10] Hayward V and Armstrong B. “A new computational model of friction applied to haptic rendering,” Experimental Robotics VI, P. Corke and J. Trevelyan, Eds., Lecture Notes in Control and Information Sciences, Vol. 250, Springer-Verlag, 2000, pp. 403-412.
- [11] Hiemenz L et al. “A Physiologically Valid Simulator for Training Residents to Perform an Epidural Block,” *Proc. 1996 IEEE Biomedical Engineering Conference*, pp. 170-173.
- [12] “Liver Biopsy.” American Liver Foundation.  
[<http://www.liverfoundation.org/html\\_filz/livheal\\_nu.htm>](http://www.liverfoundation.org/html_filz/livheal_nu.htm)
- [13] Marieb EN. Human Anatomy & Physiology, 5th ed., Menlo Park, CA: Benjamin/Cummings, 1997, pp. 920-921.
- [14] “MRC.” *ERC-CISST*. Johns Hopkins University.  
[<http://cisstweb.cs.jhu.edu/web/resources/software/mrc/>](http://cisstweb.cs.jhu.edu/web/resources/software/mrc/)
- [15] “Multi-slice Aquilion 0.5.” Toshiba America Medical Systems.  
[<http://216.23.181.196/products/product\\_family.cfm?key=12>](http://216.23.181.196/products/product_family.cfm?key=12)

- [16] Ottensmeyer MP and Salisbury, Jr. JK. “*In Vivo* Data Acquisition Instrument for Solid Organ Mechanical Property Measurement,” *Medical Image Computing and Computer-Assisted Intervention 2001*, pp. 975-982.
- [17] Payandeh S. “Force Propagation Models in Laparoscopic Tools and Trainers,” *Proc. 1997 IEEE Engineering in Medicine & Biology International Conference*, pp. 957-960.
- [18] Richard C, Cutkosky MR and MacLean K. “Friction Identification for Haptic Display,” *Proceedings of the American Society of Mechanical Engineers, Dynamic Systems and Control Division*, Vol. 67, pp. 327-334.
- [19] Stanford JL et al. “Prostate Cancer Trends 1973-1995,” *SEER Program, National Cancer Institute*. NIH Pub. No. 99-4543. Bethesda, MD, 1999.  
<http://seer.cancer.gov/publications/prostate/>
- [20] Taylor R et al. “Steady-Hand Robotic System for Microsurgical Augmentation,” *The International Journal of Robotics Research*, Vol. 18, No. 12, 1999, pp. 1201-1210.
- [21] Vuskovic V et al. “Realistic Force Feedback for Virtual Reality Based Diagnostic Surgery Simulators,” *Proc. 2000 IEEE International Conference on Robotics & Automation*, pp. 1592-1598.
- [22] “What Are The Key Statistics for Liver Cancer?” American Cancer Society.  
[http://www.cancer.org/eprise/main/docroot/CRI/content/CRI\\_2\\_4\\_1X\\_What\\_are\\_th\\_e\\_key\\_statistics\\_for\\_liver\\_cancer\\_25?sitearea=&level=>](http://www.cancer.org/eprise/main/docroot/CRI/content/CRI_2_4_1X_What_are_th_e_key_statistics_for_liver_cancer_25?sitearea=&level=>)

[23] Yen P, Hibberd RD and Davies BL. "A Telemanipulator System As An Assistant And Training Tool For Penetrating Soft Tissue," *Mechatronics*, Vol. 6, No. 4, 1996, 423-436.

## **Curriculum Vita**

Christina Simone was born on May 29, 1978 in Brooklyn, New York. She attended Stuyvesant High School in New York, New York, graduating in 1996. She graduated with honors from Carnegie Mellon University in Pittsburgh, Pennsylvania in 2000, with a Bachelor of Science in Mechanical Engineering. Christina undertook graduate studies and research at the Johns Hopkins University. There, under the guidance of Dr. Allison M. Okamura, she pursued research in the area of reality-based modeling of tool-tissue interactions for use in robot-assisted percutaneous procedures. Christina culminated her studies with a Master of Science in Mechanical Engineering in 2002.

Honors and achievements include: holding the title of Engineer-in-Training in the Commonwealth of Pennsylvania (as of Spring 2000); attaining Dean's List (Spring 1999, Fall 1998); Pi Tau Sigma - National Honorary Mechanical Engineering Society, in which the position of President was held (Spring 2000); Lambda Sigma - National Sophomore Honor Society, in which a position on the Public Relations Committee was held (1997); and the National Society of Collegiate Scholars (1997).